Functionalized MXene Films with Substantially Improved Low-voltage Actuation

Shaohua Chen, Shu Fen Tan, Harpreet Singh, Liang Liu, Mathieu Etienne, Pooi See Lee

Functionalized MXene Films with Substantially Improved Low-voltage Actuation

*Shaohua Chen[1], Shu Fen Tan[1, 2], Harpreet Singh[3], Liang Liu[3], Mathieu Etienne[3], and Pooi See Lee[1]**

[1] School of Materials Science and Engineering, Nanyang Technological University, 50 Nanyang Avenue, 639798, Singapore.
[2] Facility for Analysis, Characterisation, Testing and Simulation (FACTS), Nanyang Technological University, 639798 Singapore
[3] Université de Lorraine, CNRS, Laboratoire de Chimie Physique et Microbiologie pour les Matériaux et l'Environnement (LCPME), F-54000 Nancy, France
* Corresponding author; Email: pslee@ntu.edu.sg

$Ti_3C_2T_x$ MXene film is promising for low-voltage electrochemical actuators due to its excellent electrical conductivity, volumetric capacitance, and mechanical properties. However, its in-plane actuation is limited to little intralayer strain of MXene sheets under polarization. Here we demonstrate that a simple tetrabutylammonium (TBA) functionalization of MXene improves the in-plane actuation strain by 337% and also enhances the mechanical property and stability in air and the electrolyte. Various *in situ* characterizations reveal that the improved actuation is ascribed to the co-insertion/desertion of TBA and Li ions into/from MXene interlayer galleries and inter-edge gaps that causes a large in-plane sliding of MXene sheets under negative/positive polarizations. The assembled bending actuator has a high strength and modulus and generates a peak-to-peak strain difference of 0.771% and a blocking force up to 51.5 times its own weight under 1 V. The designed soft robotic tweezer can grasp an object under 1 V and hold it firmly under 0 V. The novel sheet sliding mechanism resembling the filament sliding theory in skeletal muscles may inspire the design of high-performance actuators with other nanomaterials.

Keywords: MXene, tetrabutylammonium, ionic actuators, artificial muscles, liquid cell TEM

1. Introduction

Electrochemical actuators (ECAs, also called ionic actuators), consisting of three/two electrodes and an electrolyte, can produce a deformation/force when a low voltage (usually < 5 V) is applied. Compared to many other actuators (e.g., pneumatic, moisture, chemical, dielectric, or thermal ones)[1-8], ECAs have many advantages such as high safety (low-voltage and low-temperature operation), lightweight, small system size, good softness, and easy control[9-10]. Hence, they are promising for a variety of applications such as tactile displays[11], bionic devices[12], and soft grippers[13]. The actuation of ECAs originates from electrode volume change induced by the electron/hole injection and ion insertion/desertion as well as possible deformation of the polymer electrolyte membrane[14-17]. The key component is the active material in the electrodes, which requires high volumetric capacitance and electrical conductivity[10]. Various materials have been explored, including

conductive polymers[9, 14, 18-19], noble metal nanoparticles[20-21], and carbon nanomaterials (e.g., carbon nanotubes-CNTs).[15, 22-23] Recently, there is a growing interest in two-dimensional (2D) nanomaterials as ECA electrodes due to their ultrahigh specific surface area, strong mechanical property, and good electrical conductivity, such as graphene[24-28], graphdiyne[29], carbon nitride,[30] black phosphorene[13], metallic MoS_2[31], and MXene[12, 32-36]. Among these, $Ti_3C_2T_x$ (T is the terminal group) MXene is promising for ECAs because of its high volumetric capacitance (900/450 F cm^{-3} in an acid/base electrolyte)[37-38], excellent electrical conductivity (over 10000 S cm^{-1})[39], and favorable polar surface for wet processing and electrolyte wetting[38, 40-42].

Most MXene-based ECAs have a sandwich structure for bending and force output, relying on the in-plane strain difference of two electrodes and the device modulus. Although the $Ti_3C_2T_x$ film exhibits considerable interlayer strain (between sheets) during the cation intercalation[34, 37, 43], the intralayer strain (along single sheets) is significantly lower[33], resulting in a small macroscale in-plane strain of the film. For example, the *c*-lattice parameter of a $Ti_3C_2T_x$ film changes by around -0.50 Å, -2.1%, and +1.42% during the cathodic scan in a 1 M $MgSO_4$[37], 1M Li_2SO_4[33-34], and 1 M H_2SO_4[35] solution, respectively. In contrast, the change in intralayer strain is only ~ +0.14% in the 1 M Li_2SO_4 solution, which aligns with the minimal change in macroscale in-plane strain of the film (~ +0.064%)[33]. Likely due to this reason, the first neat MXene-based bending ECA,[35] assembled from two aligned $Ti_3C_2T_x$ films sandwiching a poly(vinyl alcohol)/H_2SO_4 electrolyte, generated a small peak-to-peak strain difference (only 0.26% under ±0.6 V, 1 mHz) compared to many other ECAs. Hybridization of MXene with specific polymers has been proven to enhance the strain difference of the bending ECAs [33]. For instance, a methylcellulose/$Ti_3C_2T_x$ (15/85 in weight) hybrid film shows much larger in-plane actuation strain than the neat MXene film due to the possible sliding of MXene sheets, and the assembled ECA generates a peak-to-peak strain difference of 0.541% under ±1 V (1 mHz)[33, 36]. However, the electrical conductivity is relatively low (36.4 S cm^{-1}). The introduction of polystyrene microspheres into the $Ti_3C_2T_x$ film improves the ion diffusion, and the resulting ECA produces a peak-to-peak strain difference of 1.18% under ±1.5 V (0.1 Hz).[36] However, the sacrificed electrode modulus leads to a low device modulus (0.246 GPa), limiting certain applications. Additionally, the shelf and service life of MXene-based ECAs is constrained by the poor stability of MXene in humid air and aqueous electrolytes. Therefore, it is urgent to enhance the in-plane actuation strain of MXene electrodes while maintaining good conductivity, modulus, and stability for developing high-performance bending ECAs.

Here, we demonstrate that the in-plane actuation strain of a $Ti_3C_2T_x$ MXene film can be substantially improved by surface functionalization with tetrabutylammonium (TBA) groups. This functionalization reduces the number of hydroxyl groups on MXene and significantly reduces moisture absorption in ambient conditions. The resulting film also shows enhanced mechanical performance as well as improved stability in water and humid air. Based on comprehensive in situ and ex situ characterizations, we proposed a novel sheet sliding mechanism that is induced by the co-(de)insertion of TBA and Li ions for improved actuation in functionalized MXene film. Furthermore, a high-modulus ECA operating in air is assembled to produce a peak-to-peak strain difference of 0.771% under ±1 V (triangular wave, 0.1 Hz) and a blocking force up to 51.5 times its own weight under 1 V. Additionally, a soft robotic tweezer is demonstrated to be capable of grasping a flower under -1V and maintaining a tight grip even when the voltage is reduced to 0 V.

2. Results & Discussion

2.1 Fabrication and structure of the TBA-MXene film

The X-ray diffraction data (Figure S1, Supporting Information) indicates the successful preparation of $Ti_3C_2T_x$ MXene from the Ti3AlC2 precursor. Previous works show that TBA hydroxide (TBAOH) has been successfully used to intercalate and exfoliate multilayered Ti_3CNT_x, V_2CT_x, or MoC_2T_x MXene, except for multilayered $Ti_3C_2T_x$[44-46]. Here we found that exfoliated $Ti_3C_2T_x$ sheets can react with TBAOH to produce TBA-functionalized MXene (denoted as TBA-MXene in this paper) via a neutralization reaction between acidic Ti-OH groups and basic hydroxide anions.[47] This is achieved by simply mixing a MXene aqueous dispersion with a TBA hydroxide aqueous solution at a TBAOH/MXene mass ratio of 20% (**Figure 1a**). After 3-min bath sonication, many small particles of aggregated TBA-MXene sheets are present (Figure 1d) due to the attachment of hydrophobic butyl chains onto MXene sheets. To evaluate the thickness change of MXene sheets, a small portion of the aggregates was re-dispersed in the mixture of water and ethanol (1:1 in weight) under ultrasonication. Atomic force microscope (AFM) images (Figure 1 b and c) show that the thickness increased from 1.71 to 2.82 nm after TBAOH treatment, confirming the attachment of functional groups on MXene sheets. Transmission electron microscope (TEM) images (Figure S2, Supporting Information) show that the aggregate is composed of crumpled/folded TBA-MXene sheets randomly stacked together. Despite this, an intact and flexible TBA-MXene film (Figure 1e) can be obtained by vacuum-assisted filtration due to water-flow-induced pressure applied to the aggregated particles. The weight increase after functionalization gives an estimated TBA/MXene mass ratio of (7.29±1.16)% in the TBA-MXene film, corresponding to a TBA/$Ti_3C_2(OH)_2$ molar ratio of (6.06±0.96)% assuming all terminal groups as -OH. Thermal gravimetric analysis (TGA, Figure S3, Supporting Information) indicates a similar mass ratio of TBA/MXene (6.69%).

SEM images (Figure 1f, g) show a coarser surface in TBA-MXene film due to the presence of aggregated particles during functionalization. However, the TBA-MXene sheets exhibit slightly improved alignment and stacking in the film, which can be ascribed to reduced repulsion force between MXene sheets after TBA-functionalization during the filtration assembly. Furthermore, the thickness of the TBA-MXene film is also greater, explaining the mass increase after functionalization. Energy dispersive X-ray spectroscopy (EDS) result (Figure S4, Supporting Information) shows the presence of N element, confirming the introduction of TBA groups in the functionalized film. The Fourier transform infrared spectra (FTIR, Figure 1h) show that the TBA-MXene film exhibits two new peaks at 2964 and 1486 cm^{-1} compared to the neat MXene film, indicating the introduction of butyl groups on MXene. X-ray photoelectron spectra (XPS) analyses (Figure 1i and Figure S5, Supporting Information) confirm a decrease in -OH groups and an increase in quaternary ammonium groups, verifying the successful grafting of TBA groups onto MXene sheets. Besides, slight oxidation of Ti atoms and fluorination of C atoms are observed in the XPS spectra, likely due to the partial degradation of Ti-C bonds during the functionalization. X-ray diffraction (XRD) data (Figure 1j) demonstrates that the TBA-MXene film shows a slightly larger (1.52 nm) interlayer distance ($d_{(002)}$) than the neat MXene film (1.46 nm) under ambient conditions. However, after heat drying the $d_{(002)}$ of neat MXene decreased to 1.12 nm, significantly smaller than that of dry TBA-MXene (1.48 nm). This indicates the introduction of TBA groups between MXene sheets, which remarkably reduces the moisture uptake compared to the neat MXene (4.47 vs. 10.8 wt%). Besides, the TBA-MXene film

exhibits sharper (002) and (006) peaks, implying a higher-ordered stacking of MXene sheets, agreeing well with the observation in the cross-sectional SEM image.

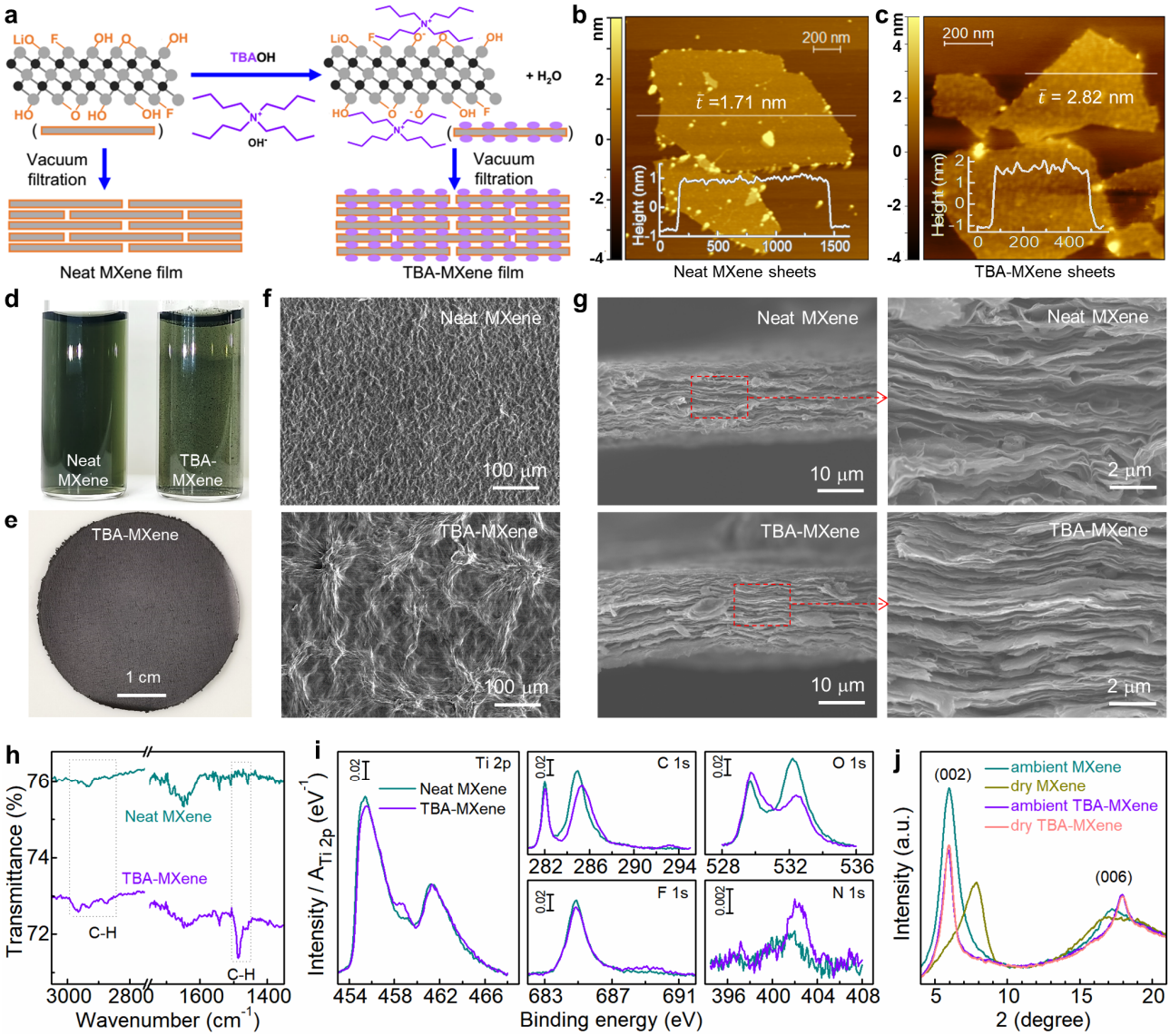

Figure 1. Fabrication and structural characterizations of neat MXene and TBA-MXene. (a) Illustration of the TBA functionalization and film formation. (b, c) AFM images of neat MXene and TBA-MXene sheets. (d) Photos of diluted neat MXene dispersion and TBA-MXene suspension (0.05 mg ml^{-1} in water). (e) Photo of a TBA-MXene film. (f, g) SEM images of (f) the top surface and (g) the cross-section of the films. (h) FTIR spectra. (i) High-resolution Ti 2p, C 1s, O 1s, F 1s, and N 1s XPS spectra normalized to the area of Ti 2p peak. (j) XRD patterns of ambient-stored (21°C, 65 RH%) and dried (80 °C under vacuum overnight) MXene-based films.

2.2 Basic performances of the TBA-MXene film

The mechanical property of MXene-based films directly impacts the actuation force and bending degree of the assembled ECA device. Tensile test results (**Figure 2a**) reveal that the TBA-MXene film assembled from the aggregated particles has a much higher tensile strength (σ = 54.6 MPa) and

elastic modulus (E = 9.49 GPa) than the neat MXene film (σ = 29.2 MPa, E = 6.65 GPa). This improvement can be attributed to the superior alignment and stacking of TBA-MXene sheets as well as much lower moisture uptake in the film. The strength and modulus of the TBA-MXene film surpass those of previous materials used for ECAs, such as ionic liquid/polymer/SWCNT composite film (σ = 17 MPa, E = 0.156 GPa)[48], PEDOT-PSS/MXene hybrid film (σ = 23.3 MPa, E = 0.668 GPa)[12], and metallic MoS_2 film (σ ≈ 17 MPa, E ≈ 2.5 GPa)[31], and are comparable to the recently reported methylcellulose/MXene hybrid film (σ = 53.2 MPa and E = 12.4 GPa). The high modulus of the TBA-MXene film enables the ECA to exhibit sufficient stiffness for some applications such as lifting operations.[31]

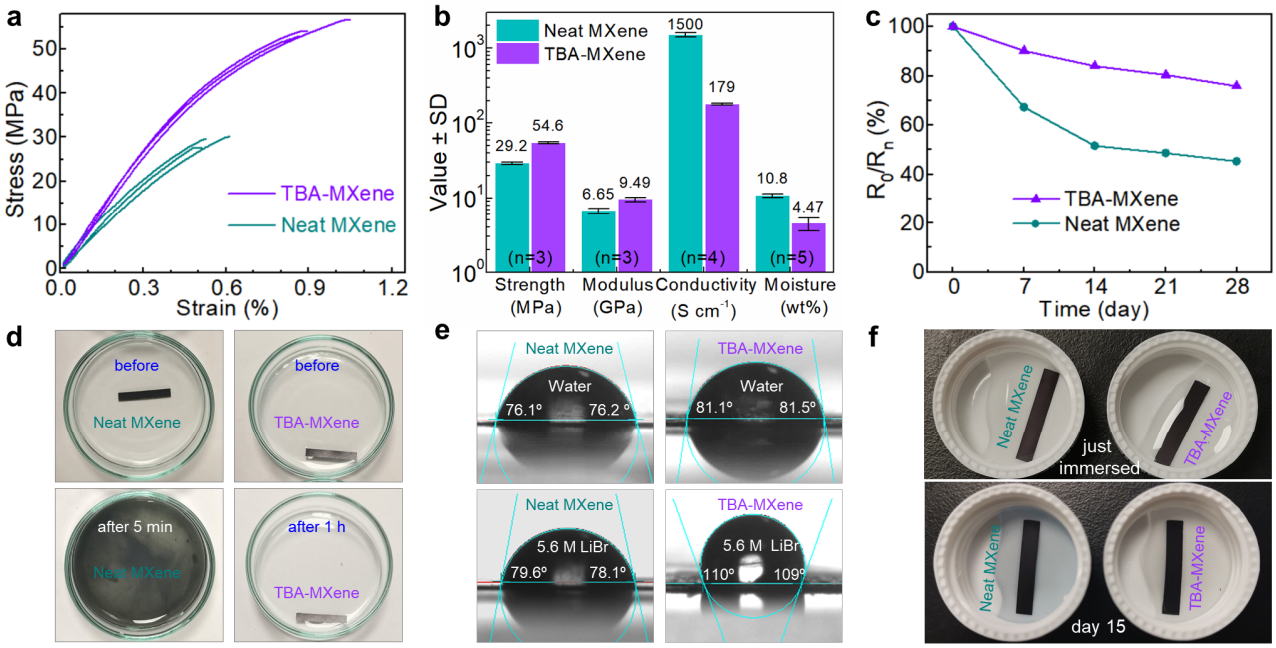

Figure 2. Basic performances of neat MXene and TBA-MXene films. (a) Tensile stress-strain curves. (b) Summary of the tensile strength, Young's modulus, electrical conductivity, and moisture uptake (moisture/dry MXene) under ambient conditions (21 °C, 65% relative humidity). (c) Retention of electrical conductivity during ambient storage. (d) Photo of the films in water before and after ultrasonication treatment (37 kHz, 330 W). (e) Contact angles of the films with water and a 5.6 M LiBr aqueous solution. (f) Photos of the films just immersed and after storage in a 5.6 M LiBr aqueous solution for 15 days.

The electrical conductivity of the TBA-MXene film (179 S cm^{-1}) is reduced compared to the neat MXene film (1500 S cm^{-1}) due to the increased interlayer distance as well as the defects in partially degraded MXene sheets and the voids in the film formed from the aggregates. Nevertheless, it is much superior to the methylcellulose/MXene hybrid (15/85 in weight: 36.4 S cm^{-1})[33] and remains within acceptable range for ECA applications. It is found that after vacuum drying at 80 °C, the conductivity is increased to 2800 and 242 S cm^{-1} for neat MXene and TBA-MXene, respectively, because of the removal of absorbed moisture. Notably, the TBA-MXene film demonstrates reduced moisture uptake (4.47 wt%) compared to the neat MXene film (10.8 wt%), thanks to the hydrophobicity of butyl groups in TBA. This leads to obviously higher retention of electrical conductivity in the TBA-MXene film (75.9%) compared to the neat MXene film (45.3%) after 28-

day storage in ambient air (21 °C, 65% relative humidity) (Figure 2c). Besides, the TBA-MXene film shows improved stability in water (Figure 2d), maintaining its shape and size under 1-hour ultrasonication treatment, while the neat MXene film quickly disintegrates after only 5 minutes. Moreover, the TBA-MXene film exhibits improved stability in a 5.6 M LiBr electrolyte solution, with minimal color change even after 15 days of immersion, unlike the neat MXene film that partially degrades to give a blue-colored product (Figure 2f). The improved stability of the TBA-MXene film in humid air, water, and the electrolyte can be attributed to the introduction of TBA groups, which increase the contact angle with water and the aqueous electrolyte (Figure 2e). These results highlight the improved stability of the TBA-MXene film in various environments, which is favorable for improving the shelf and service lives of practical actuator applications.

2.3 Electrochemical and actuation performances of the TBA-MXene film

The charge-storage and actuation behaviors of MXene-based films were evaluated in a sandwich ECA in a 5.6 M LiBr aqueous solution **(Figure 3** a and b). The ECA was assembled by sandwiching a double-sided tape with two MXene-based strips as the working electrode (WE) and counter electrode (CE). The potential of the WE is reported versus the CE, i.e., the voltage between them. The neat MXene film shows a stable cycle voltammetry (CV) curve after 6 cycles at 4 mV s^{-1}, displaying a quasi-rectangular shape with two pairs of blunt peaks (Figure 3c and Figure S6a, Supporting Information). In contrast, the TBA-MXene film requires 15 cycles to achieve a stable CV curve at 4 mV s^{-1}, exhibiting a less rectangular shape with two obvious peaks (Figure 3d and Figure S6b, Supporting Information). The CV tests were also performed in a three-electrode cell using the recorded potential range from the two-electrode cell (Figure S7, Supporting Information). In the three-electrode cell, the neat MXene displays a quasi-rectangular CV curve with a pair of blunt peaks at -0.35 and -0.05 V vs. Ag and a raised anodic tail, while the TBA-MXene gives a CV curve with clearer but more distant peaks at -0.35 and +0.1 V vs. Ag. These results indicate a combination of capacitive and pseudocapacitive charge-storage mechanisms[37, 49] in both neat and functionalized MXene films. The longer activation and less rectangular CV shape of the TBA-MXene electrode are probably due to its low affinity for the LiBr solution (Figure 2e). The stronger peaks might be ascribed to the enhanced redox activity of TBA-MXene due to the partial oxidation of MXene sheets during TBA-functionalization (Figure 1i), which exposes more Ti and C atoms for redox reactions. Note that the enhanced electrochemical activity of MXene due to partial oxidation has been observed in H_2O_2, CO_2, plasma, or anodically treated $Ti_3C_2T_x$[49-53]. At higher scan rates (Figure 3 c and d), both neat MXene and TBA-MXene films display shuttle-shaped CV curves due to limited ion diffusion into the inner part of highly in-plane aligned films.

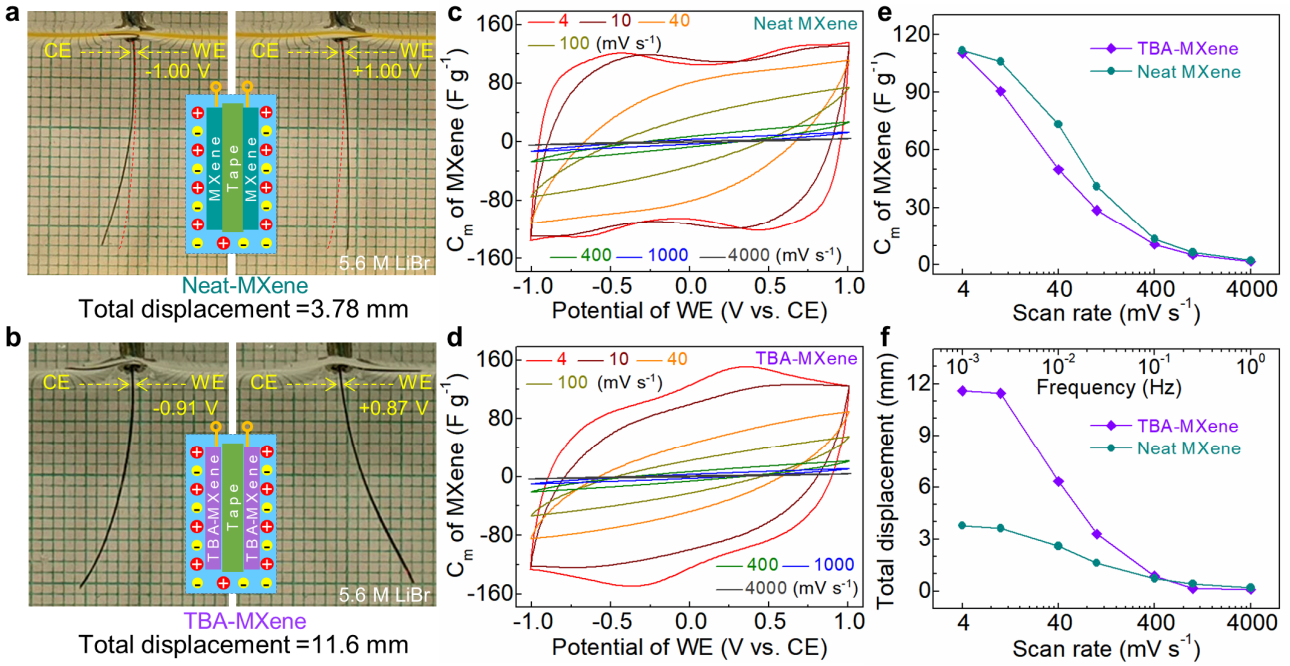

Figure 3. Electrochemical and actuation performances of neat MXene and TBA-MXene-based ECAs in a 5.6 M LiBr solution. (a, b) Photos of the ECAs at the largest bending states under different potentials. The red dashed lines in (a) indicate the position at 0 V. The largest bending of TBA-MXene-based ECA is not achieved at ±1 V because of phase delay. Insets illustrate the configuration of the ECAs. (c, d) CV curves of the ECAs under different scan rates. (e) Specific capacitance based on the mass of MXene in one electrode. (f) Dependence of the total displacement on the scan rate/frequency.

The mass-specific capacitance is calculated based on the dry mass of MXene in one film electrode. Figure 3e shows that the TBA-MXene film has comparable specific capacitance to the neat MXene film at 4, 1000, and 4000 mV s^{-1}, but lower capacitance at moderate scan rates (10-400 mV s^{-1}) due to the lower electrolyte affinity and lower electrical conductivity. Despite this, the TBA-MXene-based ECA generates significantly higher peak-to-peak (total) displacements at scan rates lower than 400 mV s^{-1} (0.1 Hz), and comparable values at higher scan rates. For example, at 4 and 10 mV s^{-1}, the total displacement of the TBA-MXene-based ECA is 2.07 and 2.17 times higher than that of the neat-MXene-based counterpart. Both ECAs show decreased displacements at higher scan rates because the in-plane aligned MXene sheets limits the ion diffusion and charge storage across the film electrode. The surprising improvement achieved by simple TBA functionalization demonstrates that the surface functional groups play a more vital role than the charge-storage capacity in the actuation performance of MXene-based electrodes. Considering that the microstructure (e.g., coarse surface and voids) of the TBA-MXene film may affect the actuation performance, we fabricated post-TBA-MXene films by treating neat MXene films with a TBAOH solution to avoid any aggregate particles in the final film. Their morphology, surface chemistry, and electrochemical and actuation performance are shown in Figure S8 (Supporting Information). SEM images show that the post-TBA-MXene film has a very similar microstructure to the neat MXene film except for the increased thickness. The XPS and XRD results confirm the successful TBA-functionalization of the neat MXene film by the post treatment. Interestingly, the post-TBA-MXene based ECAs also generate significantly higher displacements under low scan rates compared with neat MXene-based counterpart. However, under the scan rates

of 10-100 mV s^{-1} they show much lower specific capacitance and displacement than the counterpart based on pre-mixing produced TBA-MXene films. This indicates that the microstructure formed from the TBA-MXene aggregates favors the actuation under moderate frequency, attributed to the improved ion diffusion.

2.4 Actuation mechanisms of the TBA-MXene film

Various in situ and ex situ characterizations were performed to investigate the actuation mechanisms in both neat and functionalized MXene films. Firstly, the macroscale in-plane strain of the film electrode was directly monitored in a lab-made two-electrode cell (**Figure 4**a and Figure S9a, Supporting Information) during the CV test at 4 mV s^{-1} after 5-h swelling. For the neat MXene film, the in-plane strain exhibits reversible changes after two cycles of activation, especially from the 18th cycle (Figure S9c, Supporting Information), aligned with CV results (Figure S9d, Supporting Information). During the 24-26th cycle (Figure 4b), the in-plane strain increases/decreases continuously when the potential is decreased/increased from 0 to -1/+0.6 V, likely due to the electron/hole-injection and ion intercalation/deintercalation. However, the in-plane strain increases when the potential goes from +0.6 to +1 V, probably due to the oxidation of surface Ti atoms. The change in in-plane strain of the neat MXene film is +0.165% from +1 to -1 V at the 26th cycle. For the TBA-MXene film, the in-plane strain continuously increased to 0.705% during a further 2.5-h swelling before CV tests (Figure S9b, Supporting Information) due to the absorbed electrolyte. During the CV test, the baseline of the in-plane strain vs. time curve (Figure S9c, Supporting Information) increases sharply during the first 4 cycles, followed by gradual changes until the 20th cycle, consistent with the variations in CV curves (Figure S9e, Supporting Information). These changes indicated the gradual activation of the TBA-MXene film during the cycling. Figure 4b shows that the in-plane strain of the TBA-MXene film undergoes a continuous sharp increase/decrease when the potential changes from 0 to -1/+1 V, likely due to the electron/hole injection and intercalation/deintercalation of Li and TBA ions. Despite lower specific capacitance and weaker electrolyte affinity, the TBA-MXene film achieves a remarkable 0.721% change in in-plane actuation strain when the potential varies from +1 to -1 V (at the 26th cycle), 3.37 times higher than the neat MXene film. The continuous lengthening/shortening of the TBA-MXene film towards negative/positive potentials favors larger bending in the sandwich ECA due to the opposite actuation direction of the two electrodes.[33] These results highlight the advantage of TBA-functionalization and imply a novel actuation mechanism. Furthermore, assuming a constant modulus (E = 9.49 GPa) and a contraction strain (ε) of half the 0.721% under +1 V, the calculated contraction stress ($E\varepsilon$ = 34.2 MPa) and work density ($0.5E\varepsilon^2$ = 61.7 kJ g^{-1} or 159 kJ m^{-3}) of the TBA-MXene film are significantly higher than those of a metallic MoS_2 film in 0.5 M H_2SO_4 (17 MPa and 81 kJ m^{-3}).[31]

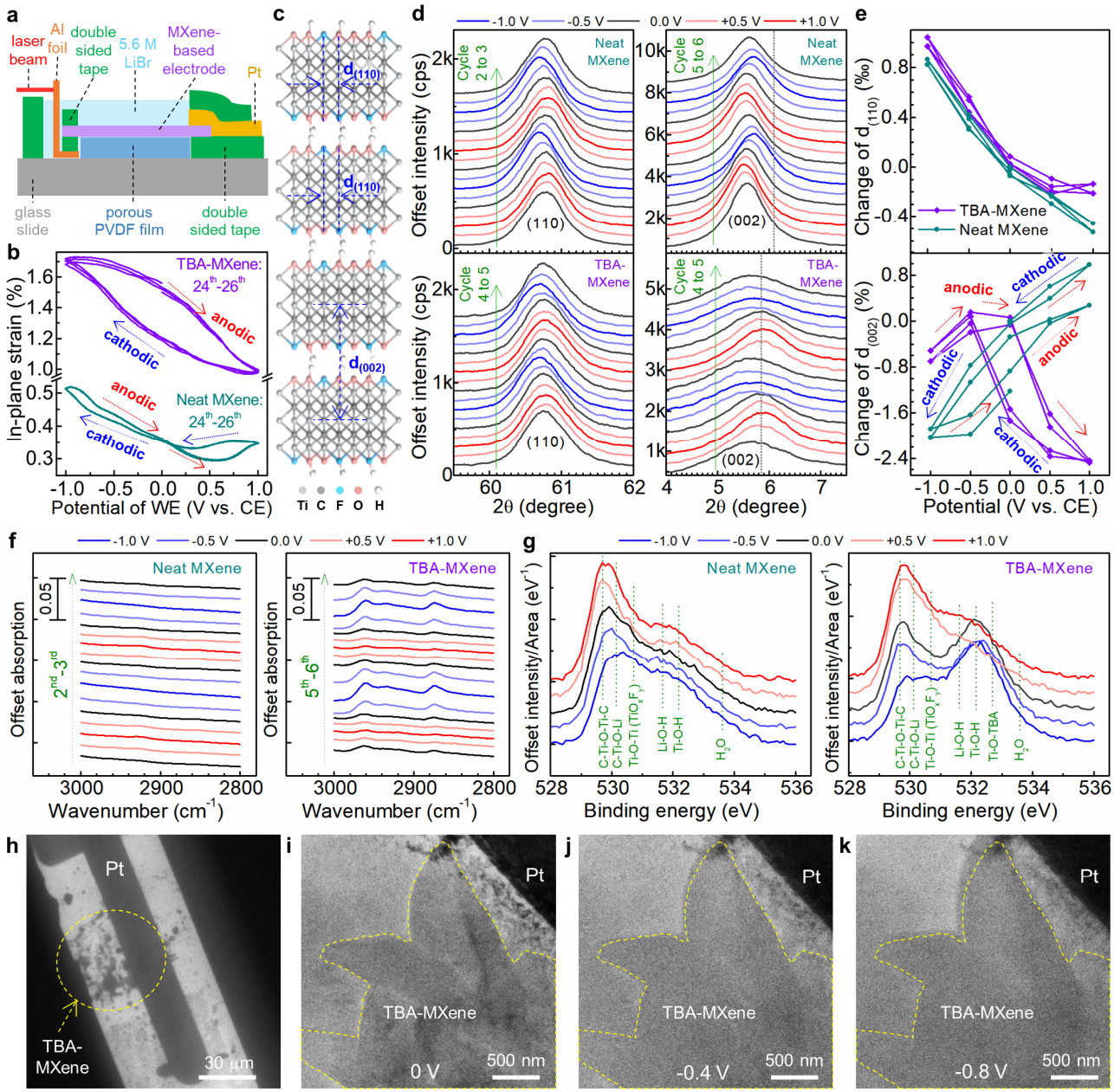

Figure 4. Investigations on the actuation mechanisms of neat MXene and TBA-MXene films. (a) Illustration of the direct measurement of the in-plane actuation strain of the working electrode (WE) by recording the horizontal displacement of the L-shaped Al foil attached to the end of the WE. (b) Dependence of the in-plane strain of the WE on the applied potentials vs. CE at 4 mV s^{-1}. Arrows indicate the scanning direction. (c) Illustration of $d_{(002)}$ and $d_{(110)}$ in MXene-based films. (d) In situ XRD patterns of the WE film at different potentials vs. CE. The dotted lines indicate the (002) peak in ambient air. (e) Changes of $d_{(002)}$ and $d_{(110)}$ of the WE at different potentials vs. the CE. (f) In situ FTIR spectra of WE films after charging to different potentials vs. the CE. (g) Ex situ O 1s XPS spectra of the electrode films biased at different potentials vs. the CE. (h-k) In situ liquid cell TEM images of TBA-MXene sheets: (h) low magnification image under no bias potential (TBA-MXene clusters reside inside the yellow dotted circle); (i-k) high magnification images under different bias potentials vs. Pt during a CV test at 20 mV s^{-1}. The yellow dotted line in (i-k) indicates the position of the profile at 0 V.

Secondly, the atomic-scale actuation strain of stacked MXene sheets in both films was probed by in situ XRD in lab-made two-electrode cells with the same electrolyte (Figure S10). As shown in **Figure 4c-e** and Figure S11 (Supporting Information), the change in (110) and (002) peaks under cyclic sweep-step potentials (Figure S11a, Supporting Information) was monitored in transmission and reflection modes, respectively, to assess the intralayer strain of single sheets and interlayer strain between sheets.[33] Both neat MXene and TBA-MXene films show comparable intensity in their (110) peaks during cycling (Figure S11 b-e, Supporting Information), with the $d_{(110)}$ values following a similar trend as the potential changes (Figure 4e and Figure S11j, Supporting Information). The change in $d_{(110)}$ indicates that under negative/positive potentials, single MXene sheets in both films undergo intralayer lengthening/shortening, resulting from the combined effects of electron/hole injection-induced elongation/contraction of the Ti-C bonds (quantum mechanical effect) and the counter-ion adsorption-induced intralayer expansion (electrostatic-double-layer effect).[15, 33] In the neat MXene film, the change in microscale strain of single MXene sheets along the [110] direction (0.135%) is slightly lower than that in the macroscale in-plane strain of the film (0.165%), indicating minimal in-plane sliding of MXene sheets. However, in the TBA-MXene film, the change in microscale strain of single MXene sheets along the [110] direction (around 0.125%) is significantly smaller than that in the macroscale in-plane strain of the film (0.721%), implying a considerable in-plane sliding of TBA-MXene sheets during polarization.

Meanwhile, the (002) peak in both films exhibits more complex changes. For the neat MXene film, after 4-h swelling in the liquid cell, the (002) peak shifts to a lower 2θ angle and becomes weaker as compared to that in ambient air (Figure S11f, Supporting Information). This indicates a swelling-induced interlayer expansion and possible in-plane sliding of MXene sheets. After CV cycling and 4 sweep-step cycles, the change in the (002) peak becomes relatively reversible (Figure 4d, e and Figure S11k, Supporting Information). During the 5^{th} and 6^{th} sweep-step cycles, the interlayer distance ($d_{(002)}$) increases/decreases when the potential varies from 0 to +1/-1 V, which could be attributed to the weakened/enhanced interlayer interaction through Li-ion deintercalation/intercalation and partial oxidation/reduction of surface Ti atoms[33-34, 54]. The resulting interlayer strain change is 2.86% and 2.33% from +1 to -1 V at the 5^{th} and 6^{th} cycles, respectively, over 16 times higher than that along the [110] direction (0.135%), demonstrating anisotropic actuation behavior of neat MXene sheets.

In contrast, the (002) peak of the TBA-MXene film shows negligible 2θ shift but significantly decreased intensity after 8 hours of swelling in the liquid cell compared to that in ambient air (Figure S11h, Supporting Information). This implies that the 5.6 M LiBr electrolyte has limited intercalation between TBA-MXene sheets due to poor affinity, but it can fill the hydrophilic inter-edge gaps and cause the sheets to slide apart, resulting in greatly reduced diffraction intensity. This is supported by the considerable increase in in-plain strain of the TBA-MXene film during swelling (Figure S9b, Supporting Information). After CV activation, the (002) peak shifts to a lower 2θ angle and becomes weaker and broader (Figure S11h, Supporting Information), indicating a slightly increased interlayer distance and further sliding of TBA-MXene sheets. This observation aligns with the increase in-plane strain of the TBA-MXene film during initial CV cycles (Figure S9c, Supporting Information). After 4 sweep-step cycles, the (002) peak presents relatively reversible changes (Figure 4d-e and Figure S11 h and k, Supporting Information). In contrast to the neat MXene film, the TBA-MXene film undergoes interlayer contraction/expansion when the potential varies from 0 to +1/-1 V, ascribed to

the co-deintercalation/intercalation of Li ions and large-sized TBA ions. The contraction from -0.5 to -1 V may result from increased interlayer interaction due to intercalated Li ions or partial chemical reduction of surface groups.[33, 54] The generated actuation-strain changes along the [002] direction are 1.86% and 1.78% from +1 to -1 V at the 4th and 5th cycles, respectively, over 13 times greater than that along the [110] direction (0.125%). This demonstrates that the TBA-MXene film also shows an anisotropic actuation behavior. Meanwhile, the (002) peak intensity of the TBA-MXene film is obviously decreased/increased when the potential varies from 0 to -0.5/+0.5 V, implying possible intercalation/deintercalation-induced sliding of MXene sheets away from/close to each other. This contributes to significant macroscale in-plane lengthening/shortening of the film. Additionally, the TBA-MXene film exhibits a lower interlayer distance than the neat MXene film under all potentials (Figure S11k, Supporting Information), suggesting that hydrated Li ions may preferably insert into the hydrophilic inter-edge gaps rather than the electrolyte-phobic galleries between TBA-MXene sheets, causing them to slide away from/close to each other under negative/positive potentials.

Thirdly, the surface chemistry of neat MXene and TBA-MXene films during the sweep-step potential treatment in a two-electrode cell was studied by in situ FTIR spectroscopy (Figure 4f) and ex situ XPS analysis (Figure 4g and Figure S12, Supporting Information) after CV cycling activation. Unlike the neat MXene electrode, the TBA-MXene film shows obvious changes in infrared absorption from 3000 to 2800 cm^{-1} during the polarization. When the potential varies from 0 V to +1/-1 V, the peaks at 2960 and 2874 cm^{-1} (ascribed to the butyl groups) become much weaker/stronger, implying the desertion/insertion of TBA cations from/into the TBA-MXene electrode. The O 1s XPS results show that the peak around 532.3 eV (attributed to Ti-OH) in the fresh MXene film (Figure 1e) become significantly weaker after cycling activation (Figure 4g, under 0 V), indicating that many protons on fresh MXene sheets are exchanged by Li ions in the 5.6 M LiBr electrolyte. For the cycled neat MXene film, the main O 1s peak around 529.9 eV under 0 V (attributed to Ti-O-Ti/Li) becomes stronger/weaker at + 1 V/-1V, while the peak around 532 eV under 0 V (attributed to Ti-OH and Li-OH) shows an opposite behavior. Simultaneously, the main Ti $2p_{2/3}$ peak at 455.4 eV under 0 V (attributed to C-Ti-C/O/F) shifts slightly to 455.6/455.2 eV under +1/-1 V (Figure S12a, Supporting Information). These findings indicate that some surface Ti atoms are oxidized to produce Ti-O-Ti under +1 V and reduced to generate low-valent Ti atoms (connected with O-vacancy and -OH) under -1 V. For the cycled TBA-MXene film, the Ti 2p peaks (Figure S12b, Supporting Information) show similar changes to those o neat MXene, indicating partial oxidation/reduction of surface Ti atoms on TBA-MXene sheets under +1/-1 V. Notably, the O 1s spectrum (Figure 4g and Figure S12d, Supporting Information) exhibits more obvious changes: the peak at 529.8 eV under 0 V (attributed to Ti-O-Ti/Li) increases/decreases obviously under +1/-1 V, while the peak at 532.1 eV (attributed to Ti-OH, Li-OH, and Ti-O-TBA) shows the opposite trend. This indicates that large-sized TBA cations could be deintercalated/intercalated together with Li ions under +1/-1 V, agreeing well with the in situ FTIR results and the large interlayer expansion/contraction of the TBA-MXene film under these potentials.

Finally, the actuation of an ultrathin TBA-MXene film (around 20 nm thick, Figure S13b, Supporting Information) was observed by in situ liquid cell TEM with a 5.6 M LiBr solution as the electrolyte. As shown in Figure 4h and i, the transferred TBA-MXene thin film consists of stacked TBA-MXene sheets. Figure S14 (Supporting Information) shows that TBA-MXene sheets are stable

and almost immobile in electrolyte solution under irradiation without applied potential. The actuation of this cluster during a CV test at 20 mV s^{-1} is presented in Supplemental Movie 1 and the snapshots under different potentials vs. Pt are shown in Figure 4i-k. The top portion of the cluster profile (yellow dotted lines in Figure 4i-k) extends significantly when the potential is decreased from 0 to -0.4 V and then to -0.8 V vs. Pt. This large lateral actuation displacement corresponds well with the increased in-plane strain of the macroscale TBA-MXene film (Figure 4b), which is likely due to the co-intercalation of TBA and Li ions under negative potentials.

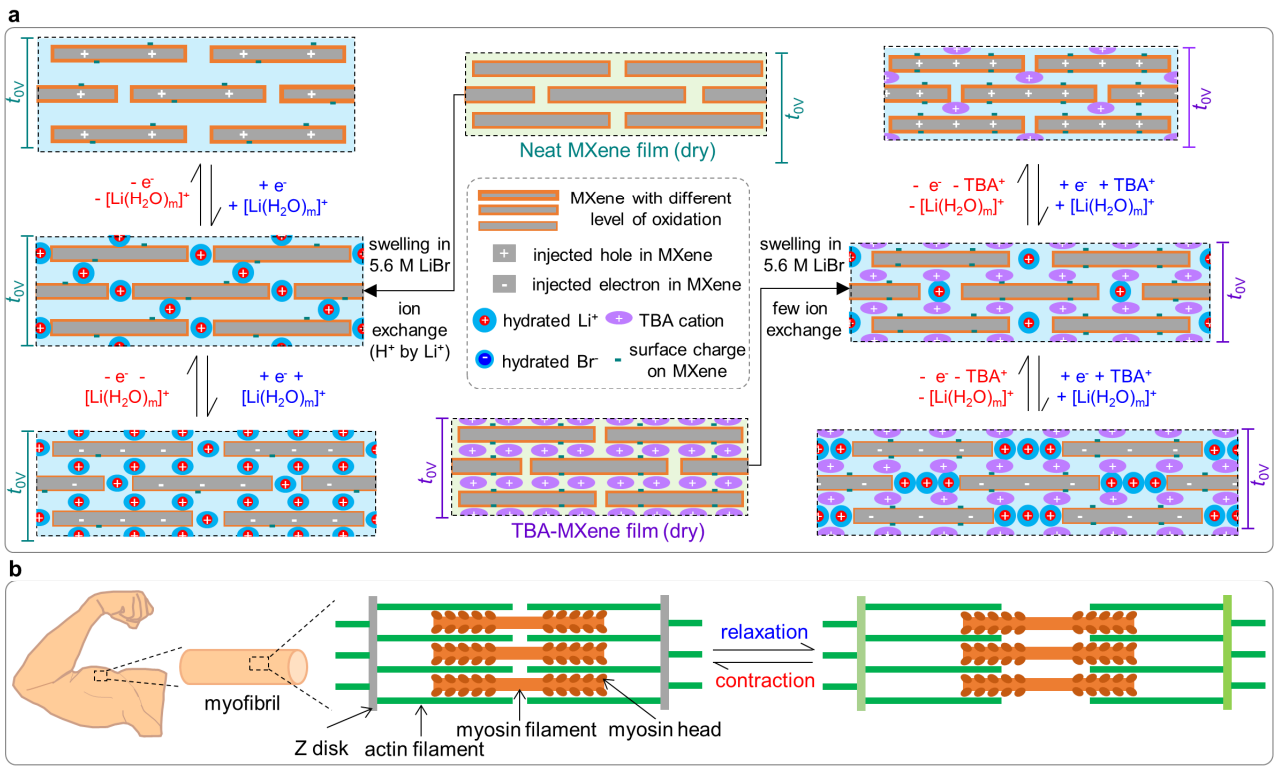

Figure 5. The proposed actuation mechanism. (a) Illustration of the proposed actuation mechanism for neat MXene and TBA-MXene films in a 5.6 M LiBr electrolyte solution. The t_{0V} indicates the thickness of the stacked sheets under 0 V (vs. CE) after cycling. The negative surface charge on MXene can be due to the dissociation of Ti-O-Li/TBA into $Ti\text{-}O^-$ in the electrolyte. For clarity, the intralayer contraction/expansion of single MXene sheets under positive/negative polarization and the presence of hydrated Br^- ions are not shown. (b) Illustration of the filament sliding model for the contraction and relaxation of skeletal muscles[55].

Considering the multi-perspective characterizations, the actuation mechanisms of neat and functionalized MXene films are discussed, as illustrated in **Figure 5a**. Under negative/positive potentials, both neat MXene and TBA-MXene sheets undergo comparable intralayer lengthening/shortening due to the injection of a similar number of electrons/holes into the MXene framework and adsorption of similar number of counter ions on the MXene surface, accompanied by partial reduction/oxidation of surface Ti atoms. However, they differ significantly in terms of interlayer and inter-edge responses to the swelling and ion (de)intercalation. The neat MXene film shows pronounced interlayer swelling in the 5.6 M LiBr solution, evident from the largely increased

interlayer distance. Its macroscale in-plane actuation strain is primarily attributed to the charge-injection-induced atomic-scale intralayer strain of single MXene sheets, with a minor contribution from in-plane sliding. The intercalation/deintercalation of Li ions in the neat MXene film induces considerable interlayer contraction/expansion but slight sheet sliding under negative/positive potentials. In contrast, the TBA-MXene film in the same electrolyte exhibit significant inter-edge swelling, indicating substantial sliding of TBA-MXene sheets away from each other due to the presence of hydrophobic butyl groups between the sheets, which repel water and reduce the interlayer interaction. The large in-plane actuation strain of the TBA-MXene film under negative/positive potentials is mildly contributed by the intralayer strain of single MXene sheets but mainly by the in-plane sheet sliding, likely caused by co-intercalation/deintercalation of large-sized TBA ions and Li ions into/from interlayer galleries and inter-edge gaps. The reduced interlayer interaction between TBA-MXene sheets could favor the sheet sliding when more TBA/Li ions are inserted into the film. The preferential insertion of hydrated Li ions into hydrophilic inter-edge gaps is expected to further enhance the sliding of TBA-MXene sheets under negative polarizations. Besides, the microstructure (e.g., coarse surface and inner voids) in the TBA-MXene film can favor the ion diffusion and charge storage to generate moderate actuation strain under mid-range frequency. Therefore, simple TBA functionalization endows the MXene film with a novel and more efficient in-plane actuation mechanism. Intestinally, the sheet sliding mechanism in the TBA-MXene film resembles the filament sliding theory governing the contraction/relaxation of mammalian skeletal muscles (Figure 5b).[55]

2.5 TBA-MXene-based ECAs working in air

An integrated ECA (IECA, **Figure 6a**) capable of working in air was assembled by sandwiching two TBA-MXene based strips with a thermoplastic polyurethane/cellulose microfiber (TPU/CMF) paper, followed by infiltration of a 5.6 M LiBr aqueous solution. This electrolyte has high wetting ability and stability in ambient conditions (21℃, 65% relative humidity) as well as higher ionic conductivity (> 150 mS cm^{-1})[56] and lower cost than typical organic ionic liquids (i.e., $EMImBF_4$). With a TPU binder, two electrodes can be well bonded to the porous CMF paper (Figure S15, Supporting Information). Thanks to the high mechanical performance of the TBA-MXene strips and the TPU/CMF paper, combined with strong interface bonding, the resulting IECA has an impressive tensile strength (σ) of 9.03 MPa and elastic modulus (E) of 1.69 GPa, surpassing most reported ECAs working in air (Table S1, Supporting information). These include ECAs based on neat MXene ($\sigma \approx$ 0.65 MPa, E ≈ 0.04 GPa),[35] MXene/(polystyrene-MXene) composite ($\sigma \approx$ 0.75 MPa, E ≈ 0.246 GPa),[36] graphdiyne/PVDF composite (σ = 5.5 MPa, E = 0.42 GPa),[29] and (phosphorene-CNTs)/CNTs composite ($\sigma \approx$ 7.7 MPa, E ≈ 0.246 GPa)[13]. Its mechanical property is also comparable to that of the recently reported methylcellulose/MXene-hybrid-based IECA (σ = 8.27 MPa, E = 1.93 GP).[33] The high mechanical performance of the TBA-MXene-based IECA is favorable for lifting or grasping applications.

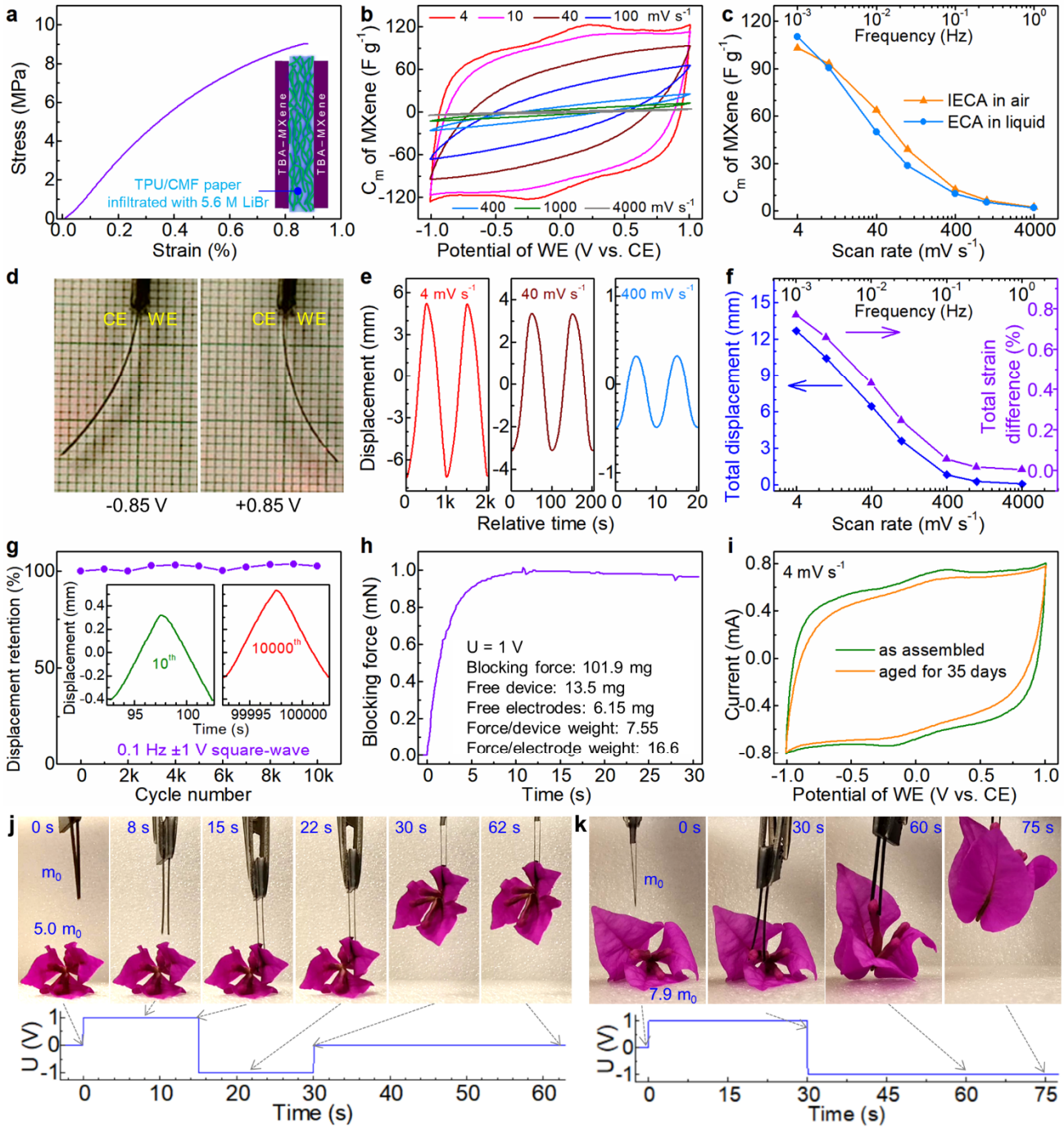

Figure 6. Performance of TBA-MXene-based IECAs working in air. (a) Tensile stress-strain curve and illustration of the device. (b) CV curves under different scan rates. (c) Dependence of specific capacitance of MXene (in one electrode) on the scan rate. (d) Photos of the IECA with maximum displacements under the indicated bias voltages (instead of -1 and +1 V due to actuation delay). (e) Displacement curves at different scan rates. (f) Dependence of the peak-to-peak (total) displacement and strain difference on the scan rate/frequency. (g) Displacement retention under a square wave (±1 V, 0.1 Hz) during the cycling. (h) Blocking force under DC 1 V. (i) CV curves at 4 mV s^{-1} of the device before and after 35-day storage in ambient conditions. (k, l) Snapshots of a two-IECA-based soft tweezer during opening and grasping a flower of (k) 5.0 times and (l) 7.9 times its own weight (based on the free part). The bottom shows the corresponding voltage profiles.

TBA-MXene-based IECA shows comparable CV curves and specific capacitances (Figure 6 b and c) to the double-sided-tape-based sandwich ECA working in the same liquid (Figure 3 d and e). Under a triangular-wave potential of ±1 V, this IECA generates a peak-to-peak displacement of 12.7, 6.45, and 0.82 mm at 0.001, 0.01, and 0.1 Hz (Supplemental Movie 2), respectively, corresponding to a peak-to-peak (total) strain difference of 0.771, 0.431, and 0.0566% (Figure 6d-f). Notably, these displacements are 44%-206% higher than those of neat-MXene-based counterpart (Figure S16, Supporting Information), despite similar stored charges. The voltage-normalized peak-to-peak strain differences also surpass those of ECAs based on gold layers,[21] CNT/PVDF films,[29] neat MXene films,[35] or methylcellulose/MXene hybrid films[33] (Table S1, Supporting information). The IECA demonstrates excellent cyclic bending stability, with a displacement retention of 102.6% after 10,000 cycles under a square-wave potential of ±1 V and 0.1 Hz (Figure 6g). Under DC 1 V, it produces a blocking force of 1.01 mN (equivalent to 7.55 times its own weight and 16.6 times the weight of two electrodes) within 10.8 s, with 80% of the maximum achieved at 3.3 s (Figure 6h). The voltage-normalized force-to-weight ratio (7.55 V^{-1}) exceeds that of previous ECAs based on methylcellulose/MXene hybrids (4.7 V^{-1})[33] or gold composite layers (~1 V^{-1}).[21] The blocking force is further improved to 1.81 mN by reducing the free length of the IECA to 6 mm (Figure S17a, Supporting Information), giving an outstanding force/weight ratio of 51.5 due to the ultrahigh modulus of the device. Scaling up the IECA width to 18 mm also increases the blocking force to 5.02 mN (Figure S17 b and c, Supporting Information). After 35-day storage in ambient conditions (21 °C, 65% relative humidity), the TBA-MXene-based IECA shows a capacitance retention of 90% at 4 mV s^{-1} (Figure 6i), thanks to the TBA functionalization. After the storage and re-activation, the displacement retention (compared at a scan rate of 40 mV s^{-1}) is 70% (Figure S18, Supporting Information), indicating the partial degradation of TBA-MXene sheets that needs to be addressed in future studies.

Finally, a low-voltage soft tweezer robot is designed (Figure S19, Supporting Information) and fabricated by mounting two TBA-MXene-based IECAs onto a trapezoid holder, allowing their ends to contact tightly. As shown in Figure 6j and Supplemental Movie 3, this tweezer can open under 1 V, grab a flower weighing five times that of two IECAs under -1 V, and hold it securely under 0 V (WE vs. CE) without loosening and damaging the flower. The firm clamping achieved 0 V is attributed to the high modulus of the TBA-MXene IECAs, providing energy-efficient transport of the grabbed object. Furthermore, this tweezer can grasp an even heavier flower (7.9 times the weight of two IECAs) and hold it steadily when -1 V is being applied (Figure 6k). These results highlight the promising potential of TBA-based IECAs for robotic applications that require softness, low-voltage operation, and energy efficiency.

3. Conclusion

The simple mixing of $Ti_3C_2T_x$ MXene with TBA hydroxide leads to TBA-functionalized MXene via a neutralization reaction. As compared to the neat MXene film, the TBA-MXene film exhibits obviously enhanced mechanical properties and improved stability in both ambient air and the aqueous electrolyte. Despite possessing a similar charge-storage capacity, the TBA-MXene film generates a substantially improved in-plane actuation strain under polarization. Based on comprehensive in situ and ex situ investigations, this enhancement is attributed to the co-insertion/desertion of TBA and Li

ions into/from MXene interlayer galleries and inter-edge gaps, which induces a considerable in-plane sliding of TBA-MXene sheets with reduced interlayer interaction. The fabricated IECA displays impressive tensile strength and modulus and can operate in air. It generates a peak-to-peak strain difference of 0.771% under a triangular-wave potential of ±1 V and a blocking force up to 51.5 times its own weight under 1 V. The IECAs can be used to assemble low-voltage, energy-saving, and soft tweezers/grippers. This simple functionalization strategy and novel sliding-induced actuation mechanism could inspire the design of high-performance ECAs based on other active nanomaterials (e.g., CNTs and graphene). Further enhancement of the actuation performance could be achieved by incorporating nanofillers and inducing a random/vertical alignment of functionalized MXene sheets to facilitate faster response and generate higher strain. The stability of MXene-based actuators could be further improved by other analogous surface functionalization methods and the use of hydrophobic ionic liquid electrolytes.

4. Experimental Section

Preparation of MXene dispersion: $Ti_3C_2T_x$ MXene was obtained by etching Ti_3C_2Al powder in a LiF-HCl solution using a modified "MILD" method.[33, 45] In a 100-ml plastic container, 4.8 g LiF (Sigma-Aldrich), 3 g Ti_3AlC_2 (≥98%, Famouschem Technology), and 15 ml deionized water were mixed under magnetic stirring for 5 min. Then 45 ml concentrated HCl (37%, AR, Shedelco) was slowly added in around 5 minutes. The container was capped loosely and placed in a 35-℃ oil bath for 36 hours of reaction under stirring. The resulting mixture was centrifuged at 5000 rpm for 5 min, and most of the liquid was removed. The sediment was washed with 300 ml water followed by centrifugation at 5000 rpm for 5-10 min. This wash and separation process was repeated 5 times to obtain sediment of multilayered $Ti_3C_2T_x$. Half of the sediment was diluted with deionized water to obtain a 300 ml suspension, which was purged with Ar and ultrasonicated in a water-ice bath in a sonicator (37 kHz, output 330 W) for 1 h. After centrifugation at 3000 rpm for 0.5 h, around 80% of the upper liquid was collected, yielding a $Ti_3C_2T_x$ MXene dispersion of 2.57 mg ml^{-1}. The MXene dispersion was stored in the fridge for later usage.

Fabrication of MXene-based films: A neat MXene film was fabricated by vacuum-assisted filtration of a 23.34 g MXene dispersion (containing 60.0 mg MXene) through an O_2-plasma-treated polypropylene membrane (Celgard 2500), followed by drying at 80 ℃ under vacuum for 12 h. Unless specified, the TBA-MXene films mentioned in the text were prepared by a pre-mixing method. Typically, a 23.34 g MXene dispersion was diluted with 36.66 g water and added with1.20 g TBAOH aqueous solution (1 wt%, Sigma-Aldrich), followed by stirring at 800 rpm for 15 min and bath sonication of 3 min. The resulting suspension with many small particles was filtrated and dried in the same way as the neat MXene film. The mass of TBA in the TBA-MXene film was estimated as the mass difference between the dry film and the raw MXene (60.0 mg). The average mass ratio of TBA to MXene was (7.29 ±1.16)% as calculated from 5 samples. Alternatively, a post-treatment method was used to prepare post-TBA-MXene films by immersing the neat MXene film in a 1% or 4% TBAOH solution in water-ethanol mixture (1:1 in weight) for 4 h followed by ethanol washing and vacuum drying. For a fair comparison of each performance, neat and functionalized MXene films were prepared at very close time gap (time difference ≤30 h) from the same batch of MXene stored

for the same duration in the fridge. All films were stored in Ar-filled glass vials before characterizations.

Assembly of MXene-based ECAs: Two kinds of ECAs were assembled from MXene-based strip electrodes. The first type operates in a 5.6 M LiBr solution and is fabricated by sandwiching a double-sided tape (23 mm × 3.5 mm × 0.050 mm, polyethylene terephthalate as the base, Darit) between two MXene or TBA-MXene strips (22 mm × 3 mm). The second type is an integrated ECA (IECA) designed for air operation, which is fabricated as follows. A TBA-MXene strip (22 mm × 3 mm) is laid on a PTFE plate, covered with a porous cellulose microfiber (CMF) paper (23 mm × 3.6 mm × 0.040 mm), and then coated with an 18 uL thermoplastic polyurethane (TPU)/dimethylformamide solution (5 wt%). Another TBA-MXene strip of the same size was placed on the paper, and the multilayered structure was vacuum dried at 80 ℃ for 2 hours to ensure bonding. Subsequently, the resulting sandwich was immersed overnight in a 5.6 M LiBr aqueous solution and then taken out to remove the excess liquid by tissue paper. The thickness of the TBA-MXene-based IECA is around 0.100 mm. A large area IECA of 18 mm × 21.5 mm (Figure S17b, Supporting Information) was fabricated similarly. A soft tweezer robot was assembled using two IECAs and a trapezoid support, as illustrated in Figure S19 (Supporting Information).

Characterizations: To measure the thickness of neat and functionalized sheets by an AFM (Cypher S, Asylum Research), the dilute dispersion in the mixture of water and ethanol (1:1 in weight) was drop-casted onto a freshly cleaved mica plate followed by vacuum drying. The moisture content in the film was calculated as the difference between the dry mass (after vacuum drying at 80 ℃ for 12 h) and the ambient mass (after storage at 21℃, 65 RH% for 12 h). TGA measurements were performed on a thermogravimetric analyzer (Q500, TA Instrument) at a ramp rate of 5 min^{-1} under flowing N_2. The morphology of TBA-MXene sheets was observed on a TEM (JEOL 2100F). The surface and cross-section of MXene-based films and IECAs were observed by a field-emission SEM (JEOL JSM-6340F). FTIR spectra were collected in the attenuated total reflection (ATR) mode on a PerkinElmer Frontier spectrometer. For XPS tests, the fresh films were secured to the metal holder by conductive silver paste and stored in the Ar-filled glove box until transferred to an X-ray photoelectron spectrometer (Quantera II with Al $K\alpha$ X-ray). XRD data was collected on an X-ray diffractometer (Shimadzu XRD-6000 with Cu $K\alpha$ X-ray). To compare the peak shift in ambient and dry MXene-based films, all films were adhered to a double-sided tape and sealed with a thin polyimide film before the XRD test. Tensile tests were performed on a dynamic mechanical analyzer (Q800, TA Instruments) at a strain speed of 1% and a gauge length of 10 mm. The resistance of strips was measured with a two-probe multimeter (Fluke 15B+) and was used to calculate the electrical conductivity based on the cross-sectional area observed by the SEM. Contact angles were measured with an optical contact angle measuring system (OCA 15Pro, DataPhysics).

The electrochemical performance was measured with an electrochemical potentiostat (PGSTAT128N, Metrohm Autolab). The sandwich ECAs were clamped by a pair of Pt sheets at one end, exposing a free part of 20 mm long for bending. CV tests were performed from -1 to 1 V (WE vs. CE) with scan rates from 4 to 4000 mV s^{-1}. The mass-specific capacitance (C_m) and average mass-specific capacitance ($\overline{C_m}$) of MXene in one electrode were calculated as follows:

$$C_m = 2I/(vm) \qquad (1)$$

$$\overline{C_m} = \int_{U_1}^{U_2} |C_m| dU/(U_2 - U_1) \qquad (2)$$

where I, v, m, U_1, and U_2 is the current, scan rate, dry mass of MXene in the working electrode, and lower and upper potentials, respectively. In another two-electrode cell with two identical MXene or TBA-MXene electrodes, the potential of the WE was recorded vs. a Ag wire while performing the CV test from -1 to 1 V (WE vs. CE) at 4 mV s^{-1}. Then the steady potential range of WE vs. Ag was used to perform the CV tests at 2 mV s^{-1} in a three-electrode configuration with the Ag wire as the reference electrode. The potential of the Ag wire in a 5.6 M LiBr solution was measured to be ~ -0.25 V vs. Ag/AgCl (saturated KCl solution).

The actuation displacement of the film or ECAs during CV measurements was recorded by a laser displacement sensor (ILD-2300-20, Micro Epsilon) or a smartphone camera (Huawei Mate20). The in-plane actuation strain of film electrodes was directly measured in a special two-electrode cell (Figure 4a and Figure S9a, Supporting Information) by recording the displacement of an L-shaped Al foil attached beneath the working electrode with the laser sensor. For ECAs working in the liquid electrolyte, the tip displacement was analyzed from the recorded video during the CV test. For IECAs working in air, the displacement was recorded by a laser sensor, with the beam pointing on the IECA around 17 mm away from the clamping point. The strain difference ($\Delta\varepsilon$) between two opposite sides of the ECA was estimated by the following equation:[14]

$$\Delta\varepsilon = 2t\delta/(\delta^2 + D^2) \qquad (3)$$

where t, δ, and D is the device thickness, displacement, and distance between the clamping point and the real or imaginary laser beam. The blocking force of the IECA is recorded by positioning its tip against a balance (ME204, Mettler Toledo) while applying a DC voltage of 1 V.

For in situ FTIR analyses, a two-electrode cell was constructed by sandwiching a porous PVDF membrane infiltrated with a 5.6 M LiBr solution between two MXene or TBA-MXene strips. After activation at 4 mV s^{-1} for 10 CV cycles (-1 to 1 V), the cell was pressed against the ATR diamond plate with a force of 25 units, and the FTIR spectra of the bottom electrode were collected during the polarization with a cyclic sweep-step potential (Figure S11a, Supporting Information). For ex situ XPS analyses, a two-electrode cell with two MXene or TBA-MXene strips (15 mm × 3 mm) was activated in the same electrolyte similarly. Then the cell was successively charged and maintained at 0, 0.5, and 1 V for 5 min each. After each step, the far ends (5 mm long) of the working and counter electrodes (with opposite potentials) were cut and respectively quenched in tetrahydrofuran (THF, 5 ml) for 10 min. After removal of THF, the cut portions were transferred to a glove box and attached to an XPS holder using a conductive silver paste, and the residual LiBr layer was scratched away to expose the MXene or TBA-MXene sheets. The samples were stored in an Ar-filled bottle until being quickly transferred to the XPS chamber for analysis. No calibration of the XPS data was performed because of the good grounding state.

In situ XRD measurements were performed in lab-made two-electrode cells (Figure S10) according to our previous report.[33] The electrodes were two strips of neat MXene or TBA-MXene of the same size, and the electrolyte was a 5.6 M LiBr aqueous solution. The (002) peak of the working electrode, which reflects the interlayer distance between MXene sheets, was monitored in a reflection mode while blocking the signal of the counter electrode with a porous membrane. In contrast, the

(110) peak of the working electrode, which reflects the intralayer strain of single MXene sheets, was monitored in a transmission mode while blocking the signal of the counter electrode by a nickel plate. All cells were first activated for 5-10 CV cycles (-1 to 1 V, 4 mV s^{-1}) until steady curves were observed, then biased under a sweep-step potential (Figure S11a, Supporting Information) for 6 cycles. The XRD data was smoothed by the Savitzky-Golay method and the average $d_{(002)}$ and $d_{(110)}$ were calculated according to Bragg's law using weight-averaged 2θ values of these peaks.

For in situ liquid cell TEM experiments, we used an electrochemical liquid cell (Protochips Inc., USA) which consisted of a spacer chip and an electrochemical chip patterned with three Pt electrodes, both with a 50-nm-thick SiN_x window (Figure S13a, Supporting Information). Both chips were treated with air plasma for ~40 seconds to make the SiN_x surfaces hydrophilic. A thin TBA-MXene film (~20 nm thick) on the polypropylene membrane was obtained by vacuum filtration. The size of the TBA-MXene layer was reduced by using a single-sided tape to create a small rectangular pattern. A small polyvinyl acetate film (~20 μm thick) was covered on the pattern, slightly pressed at 80 °C for 3 min, peeled off the membrane, and then transferred onto the Pt working electrode in the electrochemical chip. Finally, the chip was rinsed twice in 5 ml of acetone for 5 min each time, followed by drying under ambient conditions. A large MXene pattern (~10 nm thick, Figure S13b, Supporting Information) was transferred to the Pt counter electrode using a similar protocol to increase its capacitance. Then ~1 μl of 5.6 M LiBr aqueous solution was drop-casted onto the center of the electrochemical chip, which was then assembled with the spacer chip on the liquid cell TEM holder. After leak-checking, the liquid cell holder was inserted into a TEM (JEOL 2100-F) operated at 200 kV for in situ imaging under an incident flux below 10 e $Å^{-2}$ s^{-1}. The image series were acquired at a frame rate of 0.5-1 frame per second using Orius camera (Gatan Inc, USA) while performing electrochemical tests using a portable potentiostat (Gamry Reference 600+, USA). CV tests were run at 20 mV s^{-1} for at least 3 cycles from -0.8 to 0 V vs. Pt, corresponding to -0.85 to -0.05 V vs. a Ag/AgCl (saturated KCl solution) reference electrode in the 5.6 M LiBr solution.

Supporting Information

Supporting Information is available from the Wiley Online Library or from the author.

Acknowledgements

This work is funded by National Research Foundation of Singapore under project no. NRF2020-NRF-ANR102 MEACT. S.F.T. acknowledges support from NTU Presidential Postdoctoral Fellowship. The authors acknowledge Dr. Teddy Salim at FACTS, Nanyang Technological University, Singapore for the XPS measurements.

Author Contributions

S. C. and P. S. L. designed the research. P. S. L. supervised the research and edited the manuscript. S.C. performed most of the experiments (except the XPS and TEM operations) and data analyses and wrote most of the manuscript. S. F. T. guided the transfer of MXenes to liquid cell chips, performed the TEM experiments and TEM image analysis, and wrote the corresponding experimental part. H.

S., L. L. and M. E. participated in the discussion and gave some suggestions. All authors reviewed the manuscript.

Conflict of Interest

The authors declare no conflict of interest.

Data Availability

The data that support the findings of this study are available from the corresponding author upon reasonable request.

References

[1] R. F. Shepherd, F. Ilievski, W. Choi, S. A. Morin, A. A. Stokes, A. D. Mazzeo, X. Chen, M. Wang, G. M. Whitesides, *Proc. Natl. Acad. Sci. U.S.A.* **2011**, 108, 20400.

[2] H. Arazoe, D. Miyajima, K. Akaike, F. Araoka, E. Sato, T. Hikima, M. Kawamoto, T. Aida, *Nat. Mater* **2016**, 15, 1084.

[3] P. Chen, Y. Xu, S. He, X. Sun, S. Pan, J. Deng, D. Chen, H. Peng, *Nat. Nanotechnol.* **2015**, 10, 1077.

[4] Y. Shi, E. Askounis, R. Plamthottam, T. Libby, Z. Peng, K. Youssef, J. Pu, R. Pelrine, Q. Pei, *Science* **2022**, 377, 228.

[5] B. Narayan, J. S. Malhotra, R. Pandey, K. Yaddanapudi, P. Nukala, B. Dkhil, A. Senyshyn, R. Ranjan, *Nat. Mater* **2018**, 17, 427.

[6] B. Chen, T. Li, Q. Dong, E. Mosconi, J. Song, Z. Chen, Y. Deng, Y. Liu, S. Ducharme, A. Gruverman, F. D. Angelis, J. Huang, *Nat. Mater* **2018**, 17, 1020.

[7] Y. S. Kim, M. Liu, Y. Ishida, Y. Ebina, M. Osada, T. Sasaki, T. Hikima, M. Takata, T. Aida, *Nat. Mater* **2015**, 14, 1002.

[8] J. He, M. Ren, L. Dong, Y. Wang, X. Wei, B. Cui, Y. Wu, Y. Zhao, J. Di, Q. Li, *Adv. Fiber Mater.* **2022**, 4, 1256.

[9] W. Lu, A. G. Fadeev, B. Qi, E. Smela, B. R. Mattes, J. Ding, G. M. Spinks, J. Mazurkiewicz, D. Zhou, G. G. Wallace, D. R. MacFarlane, S. A. Forsyth, M. Forsyth, *Science* **2002**, 297, 983.

[10] S. Chen, M. W. M. Tan, X. Gong, P. S. Lee, *Adv. Intell. Syst.* **2021**, 2100075.

[11] K. Asaka, K. Mukai, T. Sugino, K. Kiyohara, *Polym. Int.* **2013**, 62, 1263.

[12] S. Umrao, R. Tabassian, J. Kim, V. H. Nguyen, Q. Zhou, S. Nam, I. K. Oh, *Sci. Robot.* **2019**, 4, eaaw7797.

[13] G. Wu, X. Wu, Y. Xu, H. Cheng, J. Meng, Q. Yu, X. Shi, K. Zhang, W. Chen, S. Chen, *Adv. Mater.* **2019**, 31, 1806492.

[14] Q. Pei, O. Inganäs, *J. Phys. Chem. A* **1992**, 96, 10507.

[15]R. H. Baughman, C. Cui, A. A. Zakhidov, Z. Iqbal, J. N. Barisci, G. M. Spinks, G. G. Wallace, A. Mazzoldi, D. De Rossi, A. G. Rinzler, O. Jaschinski, S. Roth, M. Kertesz, *Science* **1999**, 284, 1340.

[16] S. Nemat-Nasser, Y. Wu, *J. Appl. Phys.* **2003**, 93, 5255.

[17] Q. Pei, O. Inganaes, *J. Phys. Chem. A* **1993**, 97, 6034.

[18] D. Melling, J. G. Martinez, E. W. H. Jager, *Adv. Mater.* **2019**, 31, 1808210.

[19] F. Yu, J.-H. Ciou, S. Chen, W. C. Poh, J. Chen, J. Chen, K. Haruethai, J. Lv, D. Gao, P. S. Lee, *Nat. Commun.* **2022**, 13, 390.

[20] M. Shahinpoor, Y. Bar-Cohen, J. O. Simpson, J. Smith, *Smart Mater. Struct.* **1998**, 7, R15.

[21] Y. Yan, T. Santaniello, L. G. Bettini, C. Minnai, A. Bellacicca, R. Porotti, I. Denti, G. Faraone, M. Merlini, C. Lenardi, P. Milani, *Adv. Mater.* **2017**, 29, 1606109.

[22] N. Terasawa, I. Takeuchi, *J. Mater. Chem. C* **2013**, 1, 5272.
[23] J. Mu, M. Jung de Andrade, S. Fang, X. Wang, E. Gao, N. Li, S. H. Kim, H. Wang, C. Hou, Q. Zhang, M. Zhu, D. Qian, H. Lu, D. Kongahage, S. Talebian, J. Foroughi, G. Spinks, H. Kim, T. H. Ware, H. J. Sim, D. Y. Lee, Y. Jang, S. J. Kim, R. H. Baughman, *Science* **2019**, 365, 150.
[24] J. Kim, J. H. Jeon, H. J. Kim, H. Lim, I. K. Oh, *ACS Nano* **2014**, 8, 2986.
[25] X. Xie, L. Qu, C. Zhou, Y. Li, J. Zhu, H. Bai, G. Shi, L. Dai, *ACS Nano* **2010**, 4, 6050.
[26] J. Liang, Y. Huang, J. Oh, M. Kozlov, D. Sui, S. Fang, R. H. Baughman, Y. Ma, Y. Chen, *Adv. Funct. Mater.* **2011**, 21, 3778.
[27] L. Lu, J. Liu, Y. Hu, Y. Zhang, W. Chen, *Adv. Mater.* **2013**, 25, 1270.
[28] L. Kong, W. Chen, *Adv. Mater.* **2014**, 26, 1025.
[29] C. Lu, Y. Yang, J. Wang, R. Fu, X. Zhao, L. Zhao, Y. Ming, Y. Hu, H. Lin, X. Tao, Y. Li, W. Chen, *Nat. Commun.* **2018**, 9, 752.
[30] G. Wu, Y. Hu, Y. Liu, J. Zhao, X. Chen, V. Whoehling, C. Plesse, G. T. M. Nguyen, F. Vidal, W. Chen, *Nat. Commun.* **2015**, 6.
[31] M. Acerce, E. K. Akdogan, M. Chhowalla, *Nature* **2017**, 549, 370.
[32] T. B. Sobyra, T. S. Mathis, Y. Gogotsi, P. Fenter, *ACS Appl. Mater. Interfaces* **2021**, 13, 43597.
[33] S. Chen, J. H. Ciou, F. Yu, J. Chen, J. Lv, P. S. Lee, *Adv. Mater.* **2022**, 34, 2200660.
[34] J. Come, J. M. Black, M. R. Lukatskaya, M. Naguib, M. Beidaghi, A. J. Rondinone, S. V. Kalinin, D. J. Wesolowski, Y. Gogotsi, N. Balke, *Nano Energy* **2015**, 17, 27.
[35] D. Pang, M. Alhabeb, X. Mu, Y. Dall'Agnese, Y. Gogotsi, Y. Gao, *Nano Lett.* **2019**, 19, 7443.
[36] T. Wang, T. Wang, C. Weng, L. Liu, J. Zhao, Z. Zhang, *Nano Res.* **2021**, 14, 2277.
[37] M. R. Lukatskaya, O. Mashtalir, C. E. Ren, Y. Dall'Agnese, P. Rozier, P. L. Taberna, M. Naguib, P. Simon, M. W. Barsoum, Y. Gogotsi, *Science* **2013**, 341, 1502.
[38] M. Ghidiu, M. R. Lukatskaya, M.-Q. Zhao, Y. Gogotsi, M. W. Barsoum, *Nature* **2014**, 516, 78.
[39] J. Zhang, N. Kong, S. Uzun, A. Levitt, S. Seyedin, P. A. Lynch, S. Qin, M. Han, W. Yang, J. Liu, *Adv. Mater.* **2020**, 32, 2001093.
[40] C. Zhang, L. McKeon, M. P. Kremer, S.-H. Park, O. Ronan, A. Seral-Ascaso, S. Barwich, C. Ó. Coileáin, N. McEvoy, H. C. Nerl, B. Anasori, J. N. Coleman, Y. Gogotsi, V. Nicolosi, *Nat. Commun.* **2019**, 10, 1795.
[41] Z. Zhou, P. Li, Z. Man, X. Zhu, S. Ye, W. Lu, G. Wu, W. Chen, *Angew. Chem. Int. Ed.* **2023**, 62.
[42] M. Feng, Y. Zhang, X. Zhu, W. Chen, W. Lu, G. Wu, *Angew. Chem. Int. Ed.* **2023**, 62.
[43] X. Mu, D. Wang, F. Du, G. Chen, C. Wang, Y. Wei, Y. Gogotsi, Y. Gao, Y. Dall'Agnese, *Adv. Funct. Mater.* **2019**, 29, 1902953.
[44] M. Naguib, R. R. Unocic, B. L. Armstrong, J. Nanda, *Dalton Trans.* **2015**, 44, 9353.
[45] M. Alhabeb, K. Maleski, B. Anasori, P. Lelyukh, L. Clark, S. Sin, Y. Gogotsi, *Chem. Mater.* **2017**, 29, 7633.
[46] H. Kim, B. Anasori, Y. Gogotsi, H. N. Alshareef, *Chem. Mater.* **2017**, 29, 6472.
[47] T. Sasaki, M. Watanabe, H. Hashizume, H. Yamada, H. Nakazawa, *J. Am. Chem. Soc.* **1996**, 118, 8329.
[48] K. Mukai, K. Asaka, T. Sugino, K. Kiyohara, I. Takeuchi, N. Terasawa, D. N. Futaba, K. Hata, T. Fukushima, T. Aida, *Adv. Mater.* **2009**, 21, 1582.
[49] X. Wang, S.-M. Bak, M. Han, C. E. Shuck, C. McHugh, K. Li, J. Li, J. Tang, Y. Gogotsi, *ACS Energy Lett.* **2021**, 7, 30.
[50] B. Ahmed, D. H. Anjum, M. N. Hedhili, Y. Gogotsi, H. N. Alshareef, *Nanoscale* **2016**, 8, 7580.
[51] C. J. Zhang, S. J. Kim, M. Ghidiu, M.-Q. Zhao, M. W. Barsoum, V. Nicolosi, Y. Gogotsi, *Adv. Funct. Mater.* **2016**, 26, 4143.

[52] J. Tang, T. S. Mathis, N. Kurra, A. Sarycheva, X. Xiao, M. N. Hedhili, Q. Jiang, H. N. Alshareef, B. Xu, F. Pan, Y. Gogotsi, *Angewandte Chemie* **2019**, 131, 18013.
[53] L. Guo, X. Wang, Z. Y. Leong, R. Mo, L. Sun, H. Y. Yang, *FlatChem* **2018**, 8, 17.
[54] T. Sasaki, Y. Komatsu, Y. Fujiki, *Mater. Res. Bull* **1987**, 22, 1321.
[55] H. E. Huxley, *Science* **1969**, 164, 1356.
[56] Z. Chang, X. Wang, Y. Yang, J. Gao, M. Li, L. Liu, Y. Wu, *J. Mater. Chem. A* **2014**, 2, 19444.

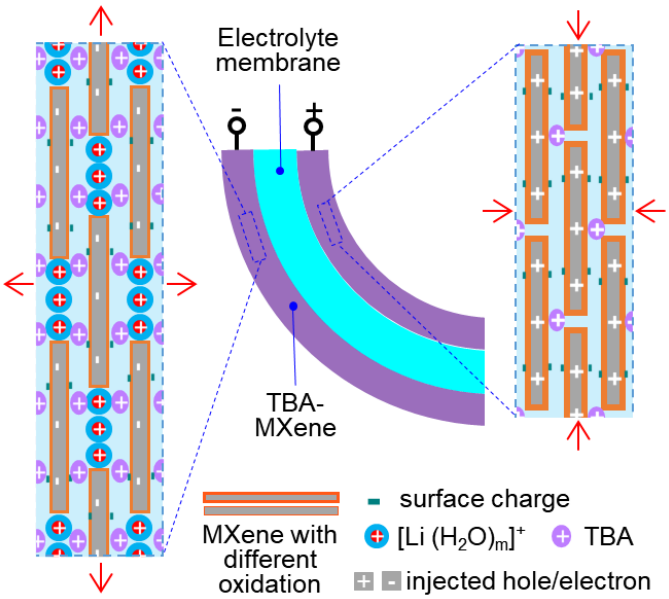
Electrolyte membrane
TBA-MXene
MXene with different oxidation
surface charge
[Li (H2O)m]+
TBA
injected hole/electron

Supporting Information

Functionalized MXene Films with Substantially Improved Low-voltage Actuation

*Shaohua Chen[1], Shu Fen Tan[1, 2], Harpreet Singh[3], Liang Liu[3], Mathieu Etienne[3], and Pooi See Lee[1]**

[1] School of Materials Science and Engineering, Nanyang Technological University, 50 Nanyang Avenue, 639798, Singapore.

[2] Facility for Analysis, Characterisation, Testing and Simulation (FACTS), Nanyang Technological University, 639798 Singapore

[3] Université de Lorraine, CNRS, Laboratoire de Chimie Physique et Microbiologie pour les Matériaux et l'Environnement (LCPME), F-54000 Nancy, France

* Corresponding author; Email: pslee@ntu.edu.sg

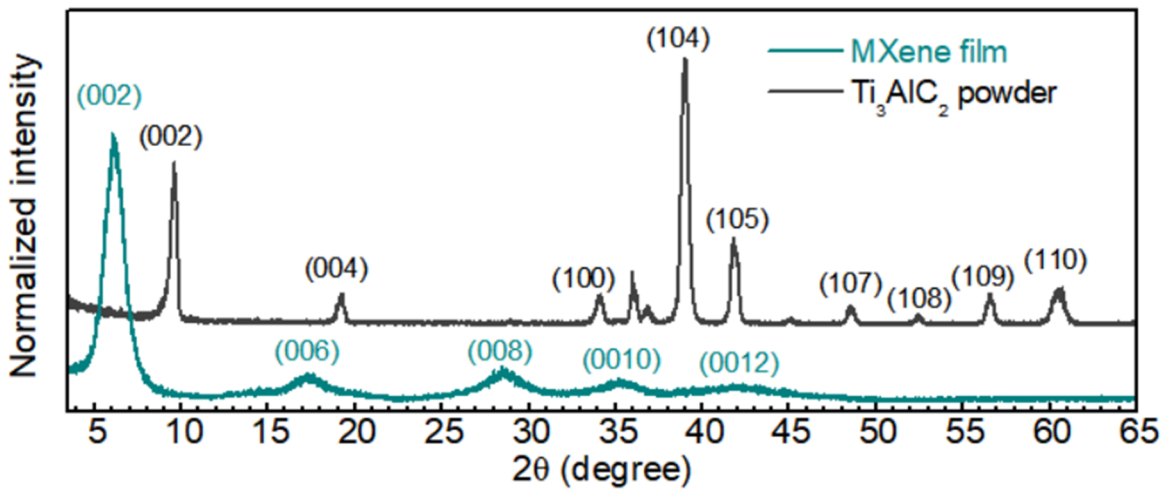

Figure S1. XRD pattern of the neat MXene film and the Ti_3AlC_2 powder.

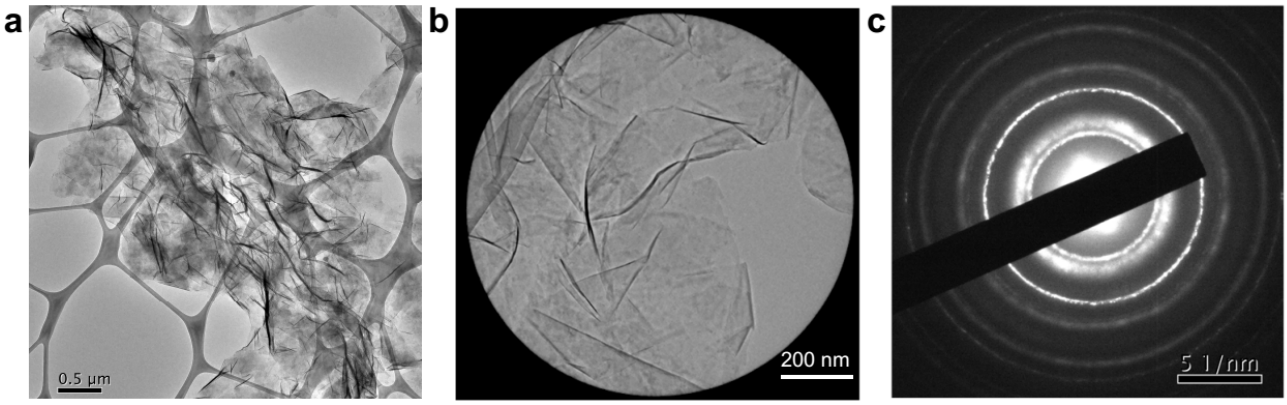

Figure S2. (a, b) TEM images and (c) corresponding selected area electron diffraction pattern of aggregated TBA-MXene sheets in (b).

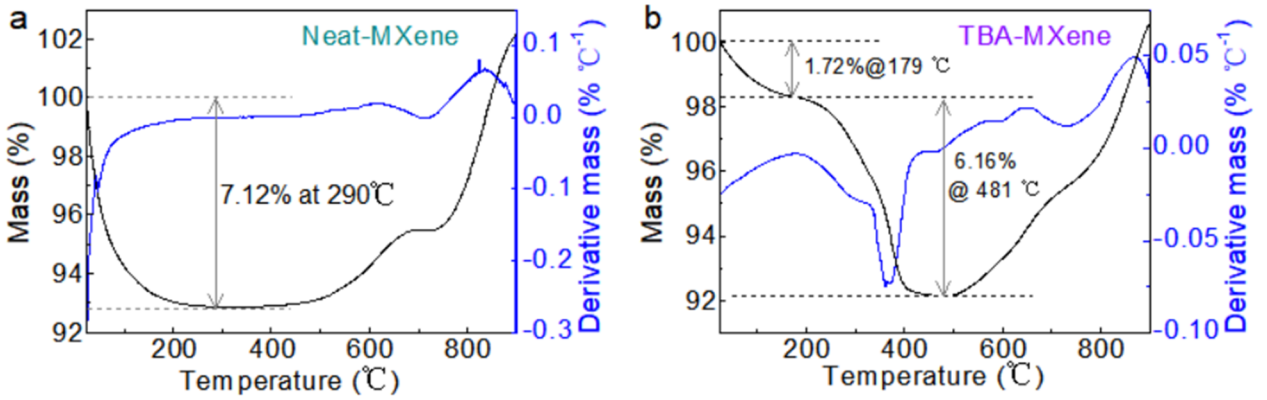

Figure S3. TGA of (a) the neat MXene film and (b) the TBA-MXene film. The neat MXene film shows a sharp mass loss below 200 ºC due to the evaporation of considerable amount of absorbed moisture. In contrast, the TBA-MXene film underwent only a slight mass loss below 200 ºC indicating little moisture absorption under ambient condition. The mass loss between 179 to 500 ºC can be ascribed to the degradation of TBA groups. The weight ratio of TBA/MXene is around 6.69 wt%, close to the value obtained by vacuum drying at 80 ºC for 12 h.

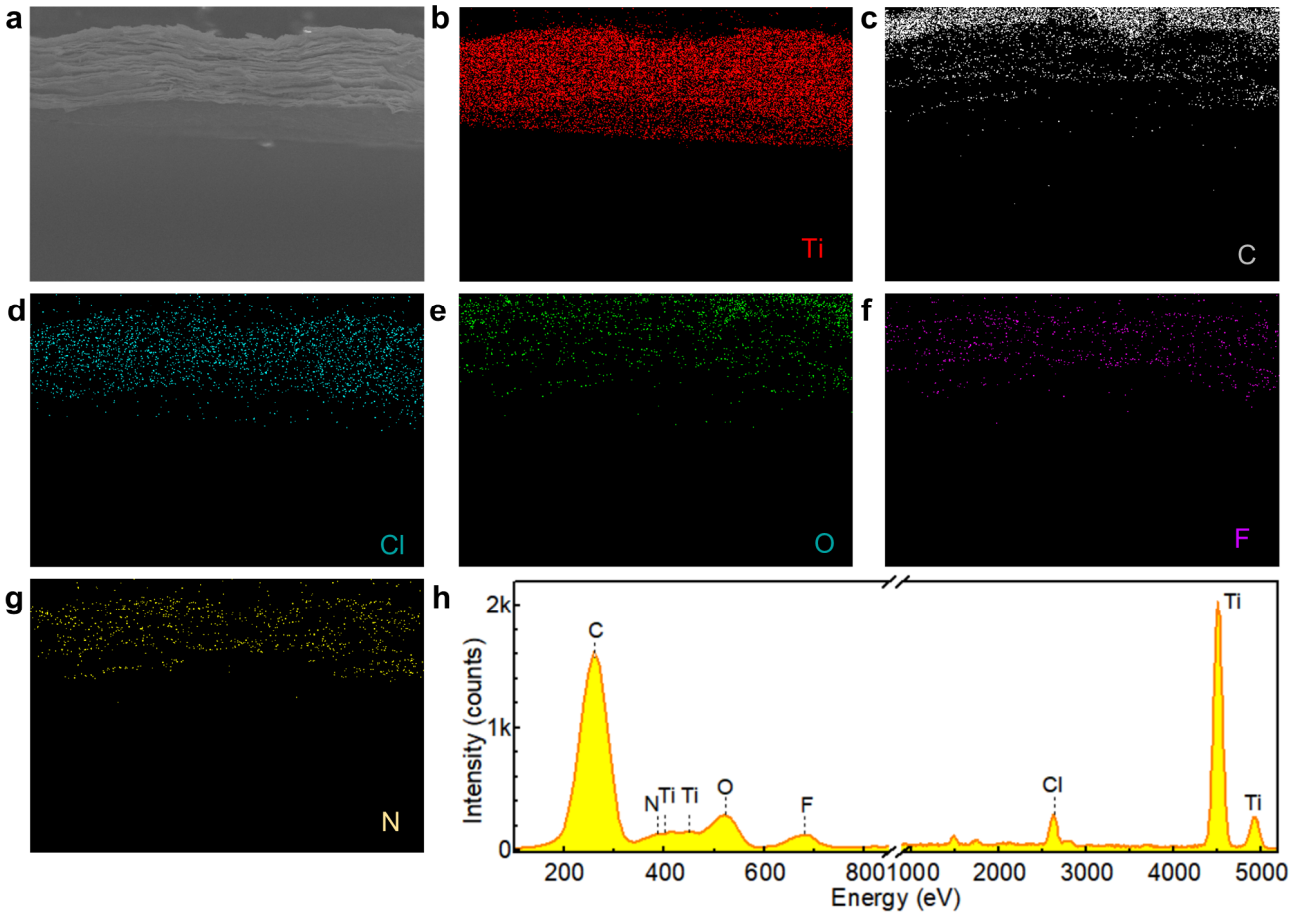

Figure S4. (a) SEM image, (b-g) corresponding EDS mapping of different elements, and (h) EDS of cross-section of a TBA-MXene film.

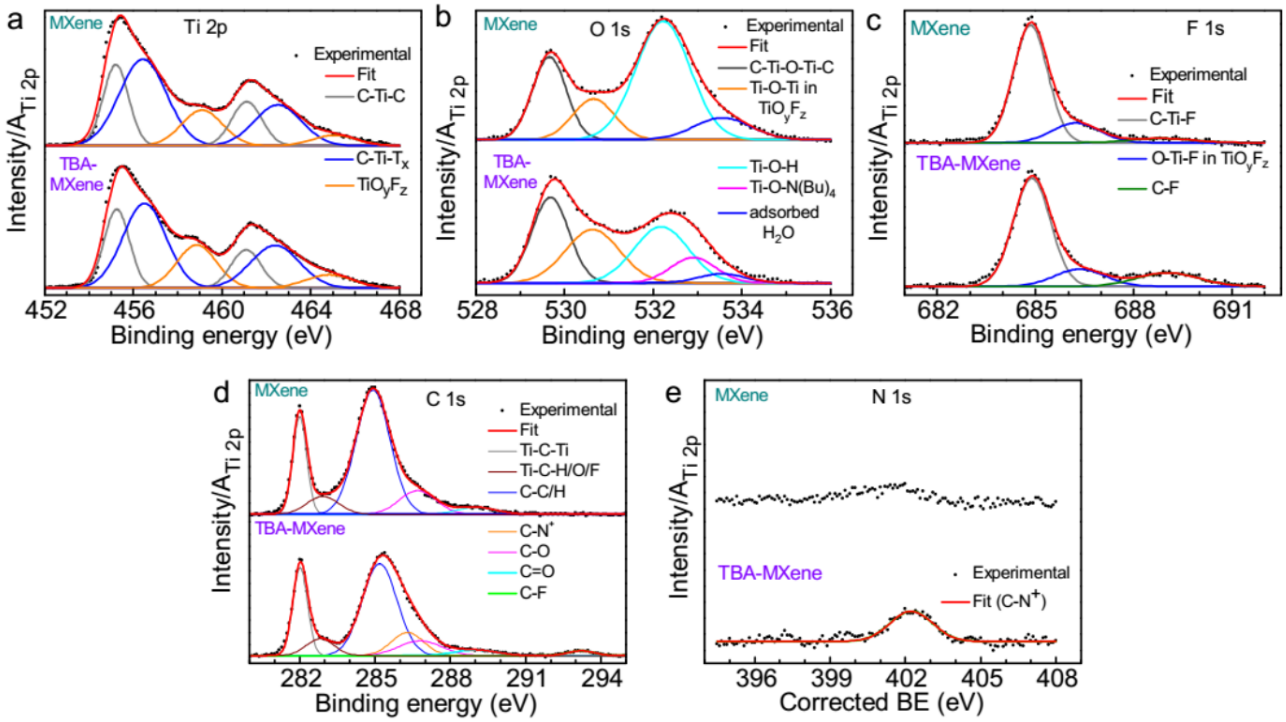

Figure S5. Deconvoluted (a) Ti 2p (T denotes terminal groups such as –O, -OH, -OLi, -O-TBA, -F and -Cl), (b) O 1s, (c) F 1s, (d) C 1s, and (e) N 1s XPS spectra of the neat MXene and TBA-MXene films. The intensity of all spectra is normalized to the area of the Ti_{2p} peak.

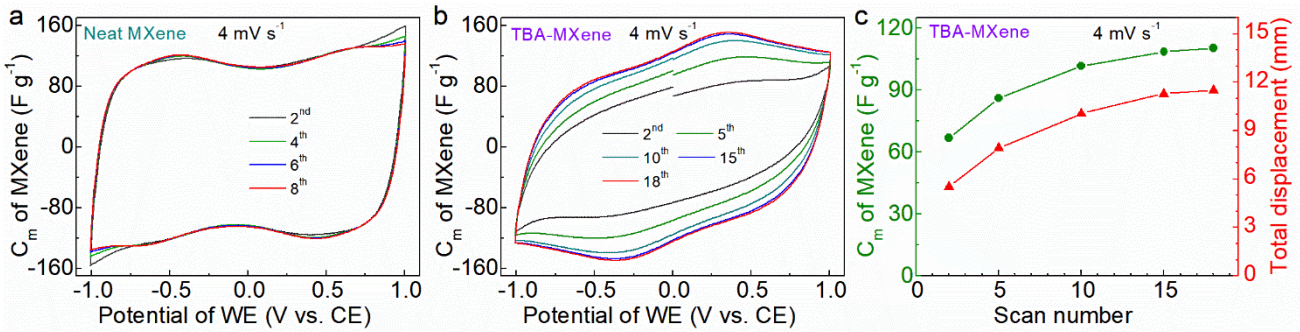

Figure S6. Supplemental data of the ECAs working in a 5.6 M LiBr solution electrolyte (as shown in Figure S3). (a,b) CV curves at 4 mV s^{-1} of (a) neat MXene and (b) TBA-MXene based ECAs. (c) Evolution of the specific capacitance and total displacement of TBA-based ECA during the CV measurement at 4 mV s^{-1}.

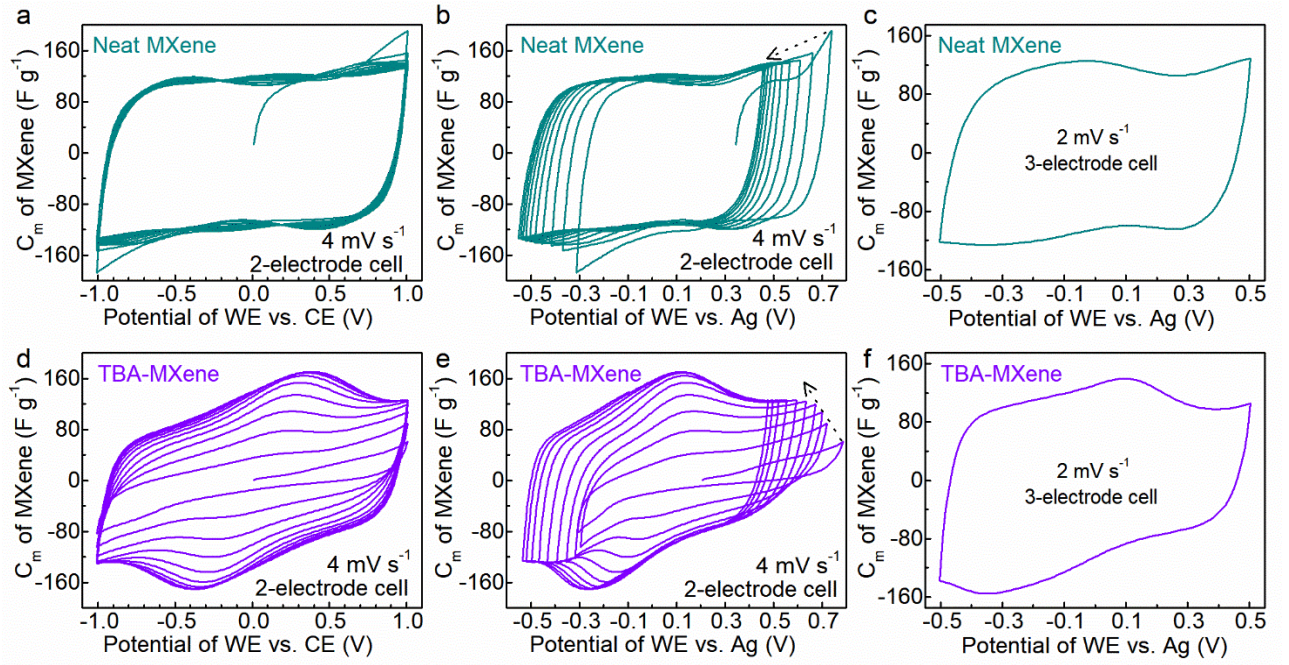

Figure S7. CV curves of (a-c) the neat MXene and (d-f) the TBA-MXene in (a, b, d, e) 2-electrode cells and (c, f) 3-electrode cells with a 5.6 M LiBr solution as the electrolyte. In all cells, the mass and size of working electrode (WE) and counter electrode (CE) were almost the same. For (b) and (e, the potential of the WE vs. a Ag wire in a 2-electrode cell was simultaneously recorded while running the CV measurements on a multichannel modular potentiostat. As shown in (b) and (e), the potential range of WE (either neat MXene or TBA-MXene) vs. Ag gradually shifts to around -0.5~+0.5 V, which was used for the CV scan in the 3-electrode cell.

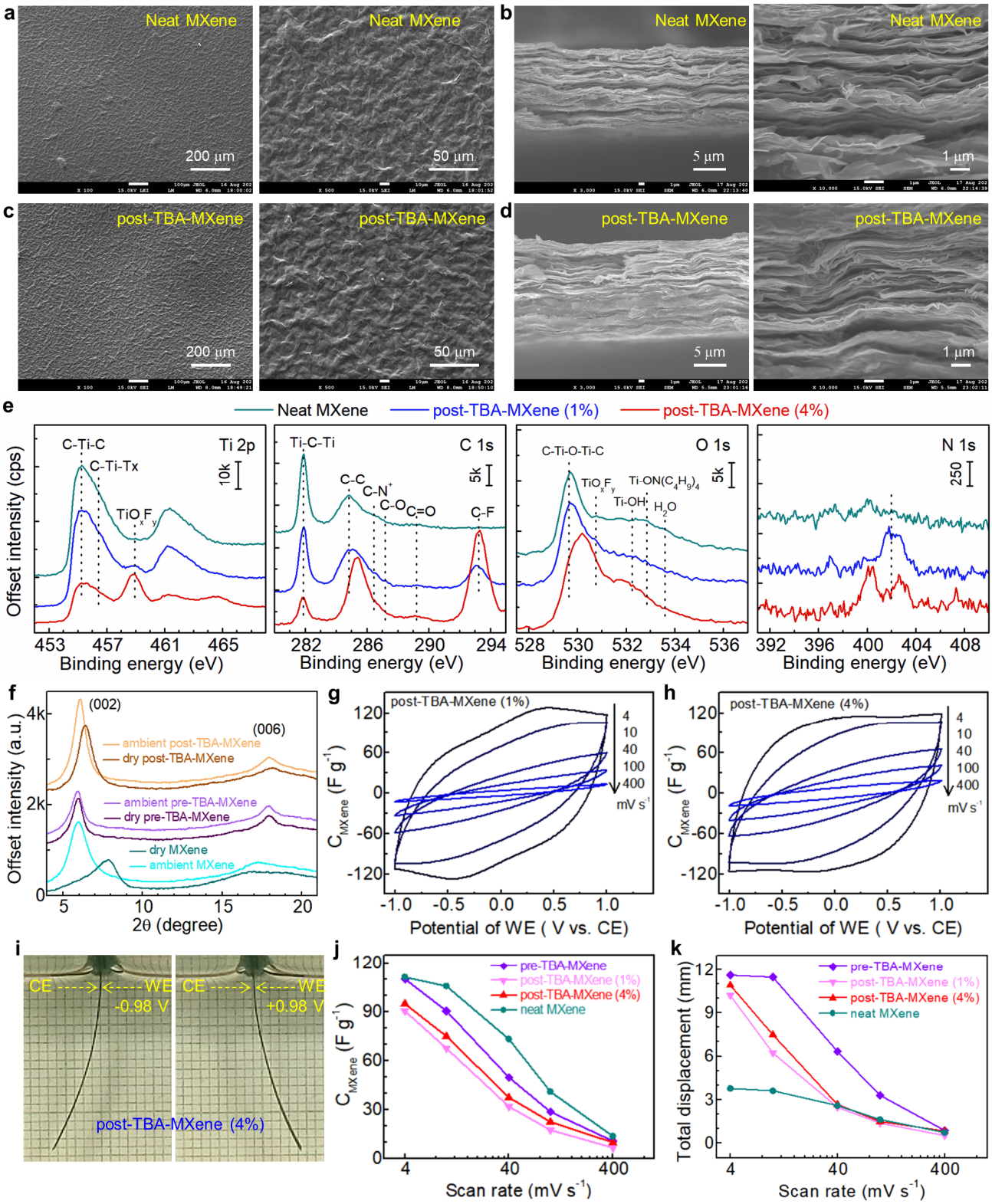

Figure S8. Characterizations of the post-TBA-MXene films. (a-d) SEM images of (a, c) the surface and (b, d) the cross-section of (a, b) the neat MXene film and (c, d) the post-TBA-MXene film (from 1% TBAOH solution). This shows that both films have very similar microstructure except that the post-TBA-MXene film has a higher thickness due to the functionalization. (e) Ti 2p, C 1s, O 1s and N 1s XPS of a fresh neat MXene strip and post-TBA-MXene strips obtained by treating the neat MXene film with 1% and 4% TBAOH solution. These strips were originated from the same piece of

fresh MXene film. (f) XRD patterns of the films in ambient and dry conditions. (g, h) CV curves of the post-TBA-MXene based ECA working in a 5.6 M LiBr solution. (i) Photo of the post-TBA-MXene (4%) based sandwich ECA. (j, k) Comparison of the single-electrode capacitance (based on the mass of MXene) and total displacement different MXene-based ECAs. Pre-TBA-MXene stands for the TBA-MXene prepared by the pre-mixing method.

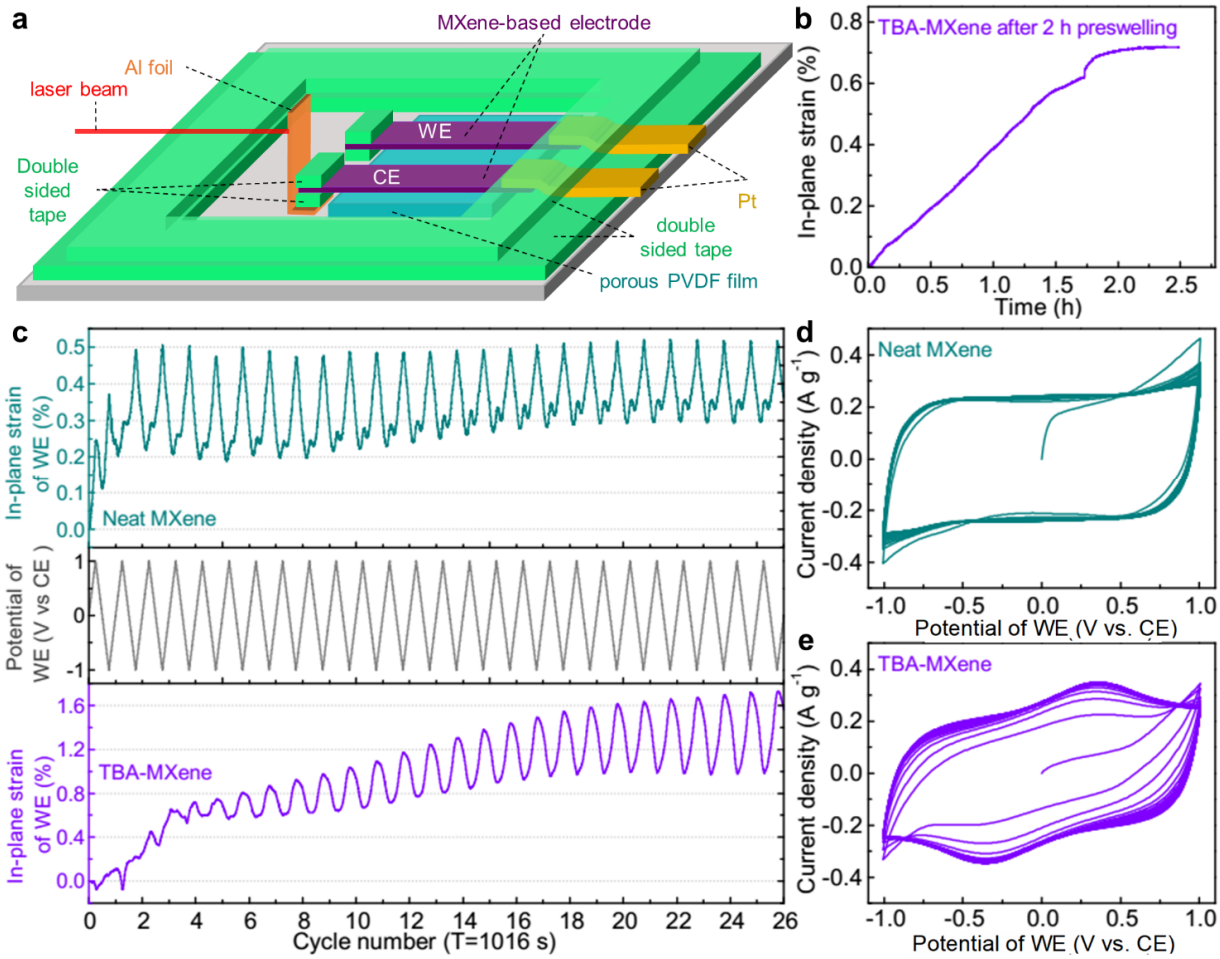

Figure S9. Supplemental data for the direct in-plane strain measurement. (a) Illustration of a two-electrode cell for the measurement. The electrolyte (5.6 M LiBr aqueous solution) is not shown. (b) Evolution of in-plane strain of a pre-swollen TBA-MXene film during the further swelling in the cell. (c) Evolution of in-plane actuation strain and potential of neat MXene and TBA-MXene working electrode during CV tests at 4 mV s^{-1} for 26 cycles. (d, e) CV curves of neat MXene and TBA-MXene based cells.

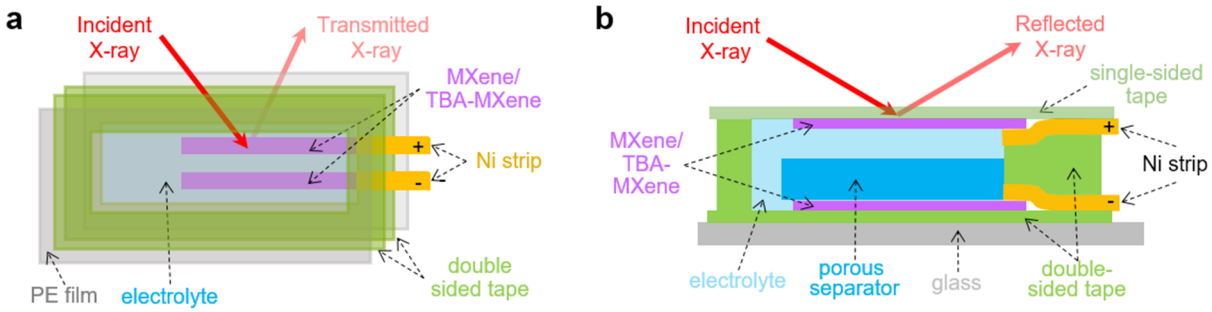

Figure S10. Illustration of in-situ XRD tests of neat MXene and TBA-MXene films in two-electrode cells. (a) The transmission mode for the (110) peak. A Nickel plate (thickness: ~ 0.1 mm) was covered on the counter electrode (the lower one) to block its (110) signal. (b) The reflection mode for the (002) peak. The porous poly(vinylidene difluoride) separator (pore size: 0.22 mm; thickness: ~0.1 mm) was confirmed effective for blocking the (002) signal of the bottom electrode.

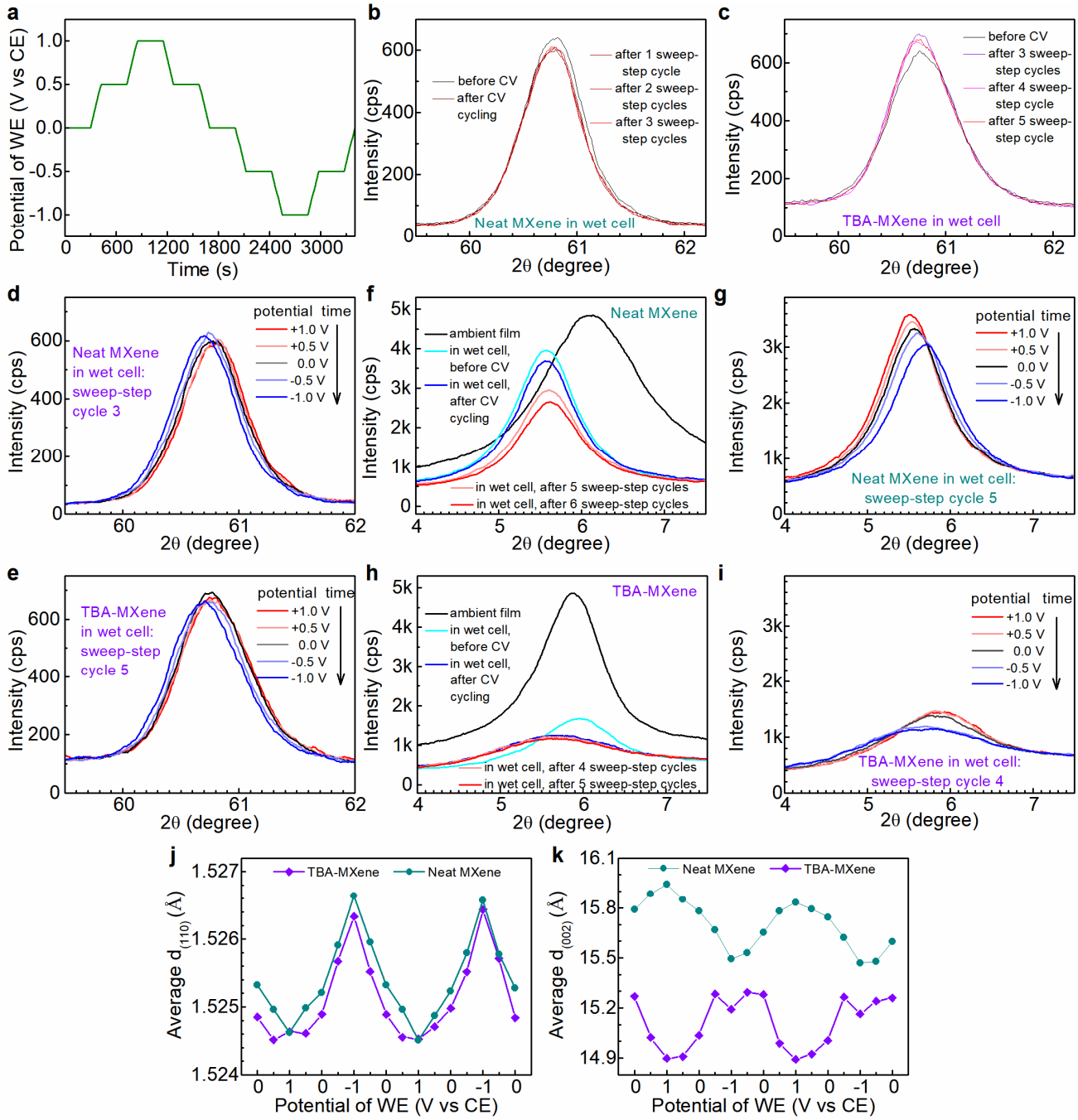

Figure S11. Supplemental data for in situ XRD investigations. (a) The sweep-step potential profile in one cycle. Each step potential was maintained for 5 min, and the sweep rate is 4 mV s^{-1}. (b, c) Evolution of the (110) peak of (b) neat MXene and (c) TBA-MXene working electrodes in the wet cell before and during CV activation and sweep-step cycling. The voltage is kept zero during these measurements. (d, e) Evolution of the (110) peak of (d) neat MXene and (e) TBA-MXene working electrodes under different step potentials vs. counter electrode in one half cycle. (f, h) Evolution of the (002) peak of (f) neat MXene and (h) TBA-MXene working electrodes in the wet cell after different CV and sweep-step cycles. The voltage is kept zero during these measurements. (g, i) Evolution of the (002) peak of (g) neat MXene and (i) TBA-MXene working electrodes under different step potentials vs. counter electrode in one half cycle. (j, k) Change of (j) $d_{(110)}$ and (k) $d_{(002)}$ of the working electrodes during the sweep-step cycles.

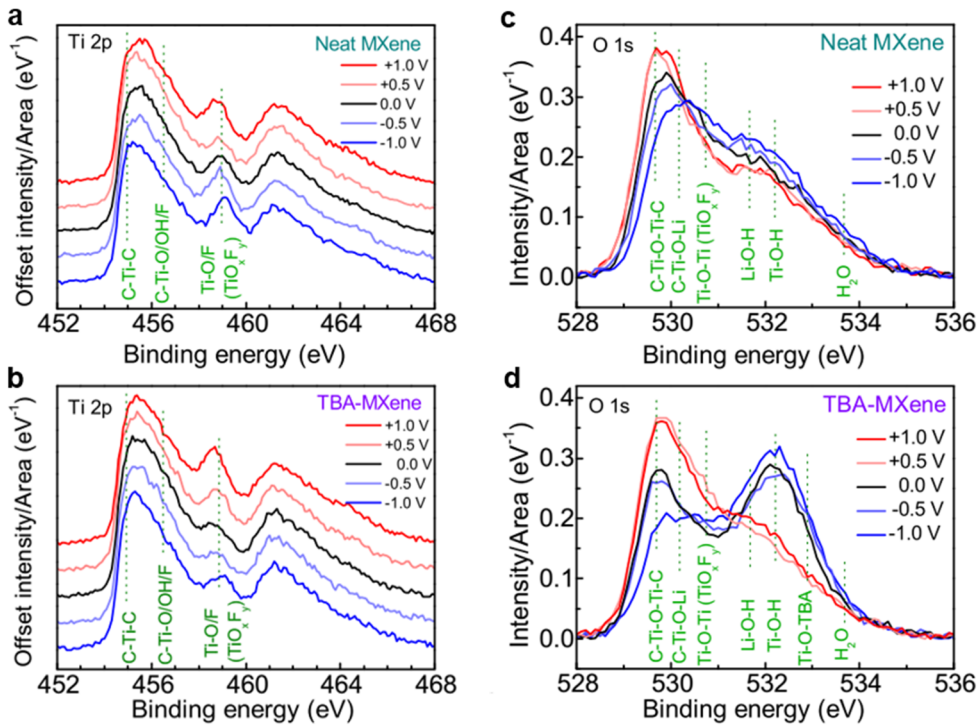

Figure S12. Ex-situ XPS spectra of the working electrode (WE) films after charging to different potentials vs. the counter electrode (CE): (a, b) Normalized Ti 2p survey; (c, d) Normalized O 1s survey.

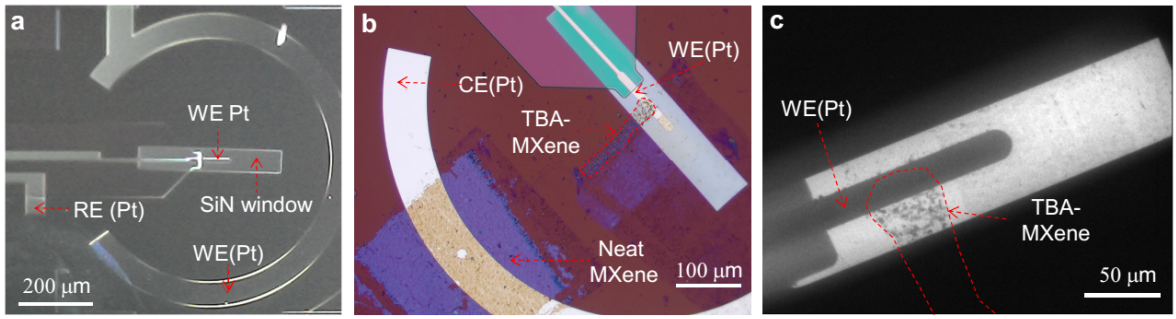

Figure S13. Set-up for in situ electrochemical liquid cell TEM experiments. (a, b) Optical images of the electrochemical chip (a) before and (b) after sample transfer (red dotted rectangle). (c) Low-magnification TEM image of the transferred sample (red dotted line).

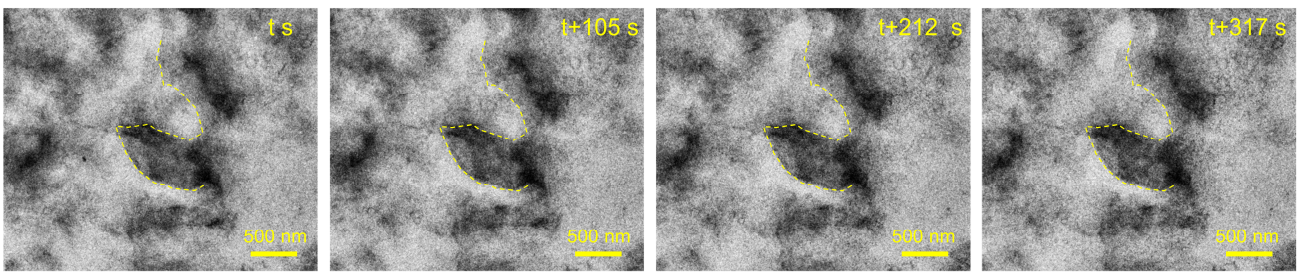

Figure S14. Sequential TEM images of TBA-MXene sheets in the liquid cell before applying a potential. The yellow dotted line indicates the position of the profile at t s. The sheets are stable under irradiation for more than 5 min.

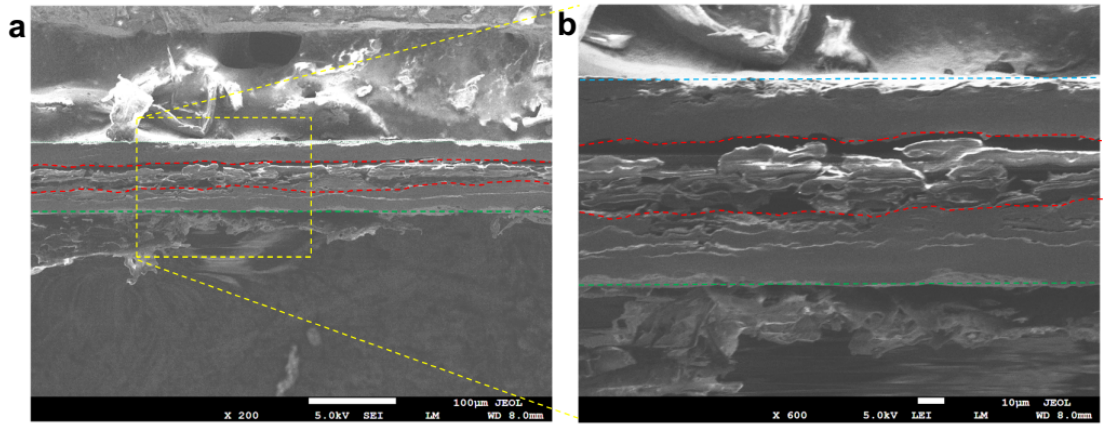

Figure S15. SEM images of the cross-section of a TBA-MXene based IECA before infiltration of the liquid electrolyte. Red dotted lines mark the interface between the TBA-MXene film and the TPU/CMF paper.

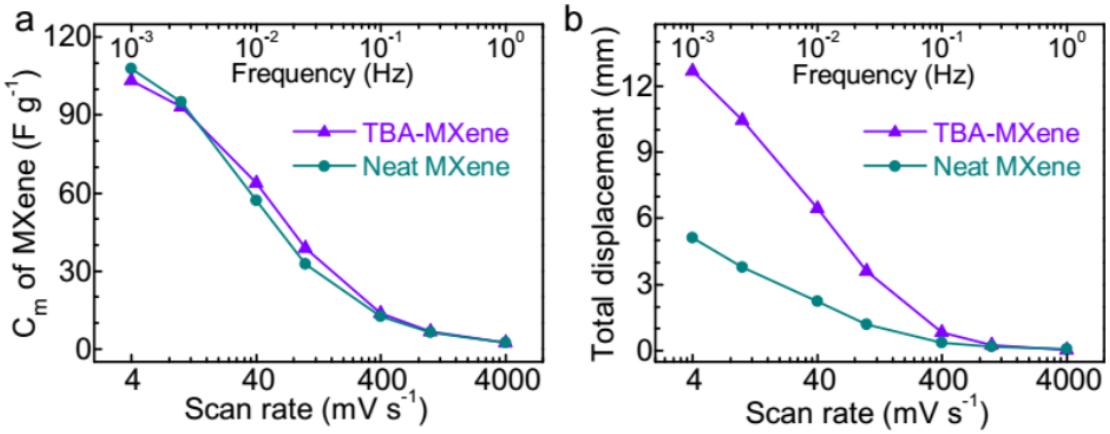

Figure S16. Comparison of the specific capacitance and total displacement of IECAs based on neat MXene and TBA-MXene under different scan rates. The free length was 17 mm.

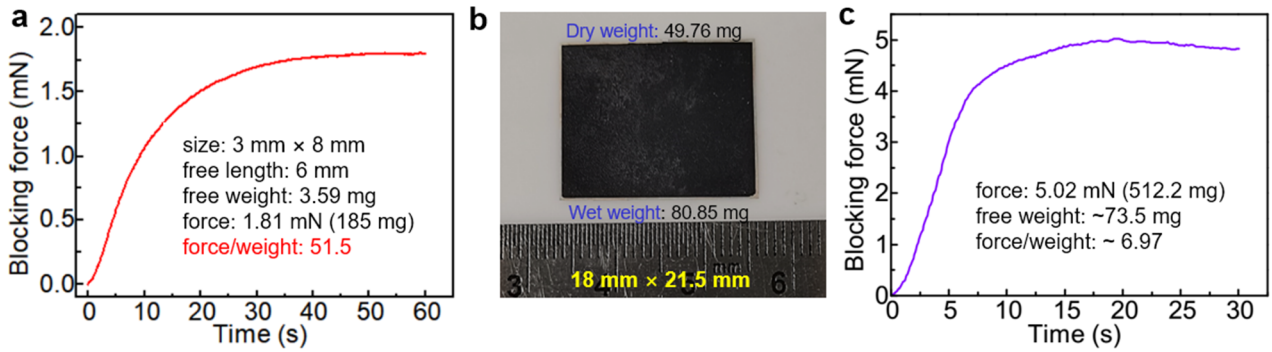

Figure S17. Performance of short and wide IECAs: (a) Blocking force of a short IECA (free length = 6 mm) under DC 1 V for 30 s. (b, c) Photo and blocking force of a wide IECA under DC 1 V for 30 s.

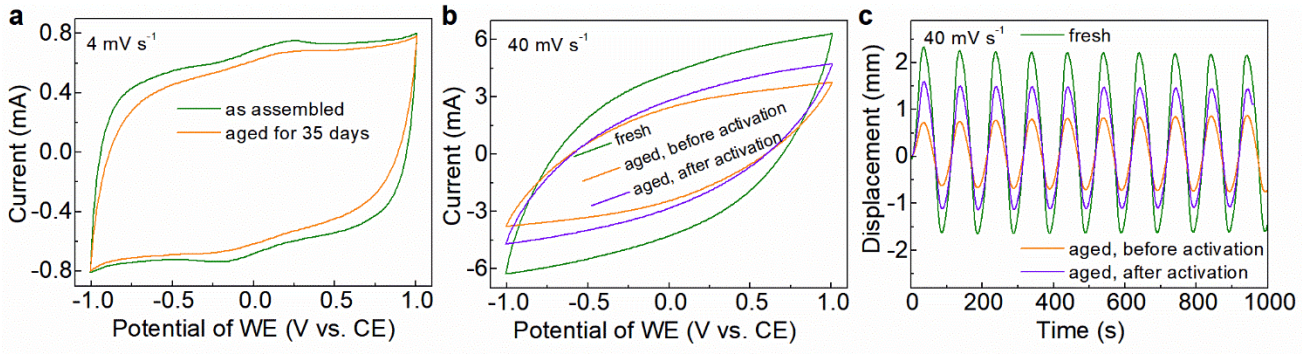

Figure S18. Effect of aging in ambient condition (21 °C, 65% relative humidity) on the performance of TBA-MXene based ECA: (a) CV curves at 4 mV s^{-1} before and after 35-day aging; (b) CV curves at 40 mV s^{-1} before and after 35-day aging. The activation was done by running a CV at 4 mV s^{-1} for 10 cycles; (c) Actuation displacement of fresh and aged device at 40 mV s^{-1} under a triangle wave of ± 1V and 0.01 Hz.

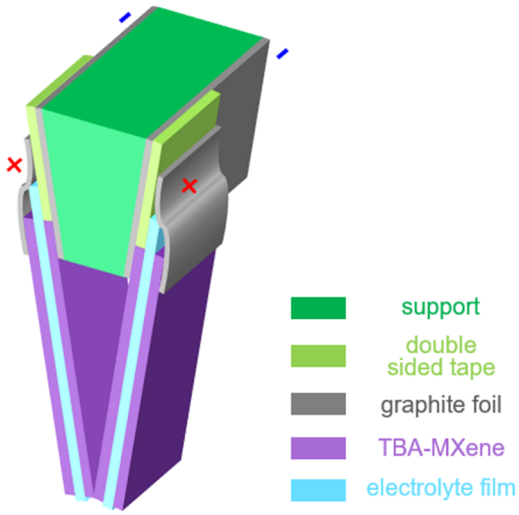

Figure S19. Illustration of a soft tweezer composed of two TBA-MXene based IECAs with the ends touching each other.

Table S1. Summary of ECAs based on MXene and other inorganic materials.

Ref.	Electrode parameters			Device parameters						
	Component	Strength [MPa]	Elastic modulus [GPa]	Electrolyte membrane	Device modulus	Applied voltage [V]	Device Size [a] [mm^3]	Peak-to-peak $\Delta\varepsilon$/Voltage [% V^{-1}]	Blocking force/ Voltage [mN V^{-1}]	(Force/ Weight)/ Voltage [V^{-1}]
[1]	Deposited Au layer	—[b]	—	$EMIBF_4$/ HNC/PAA-co-PAN	0.00035	±5	25×2.5× 0.35	0.208 (0.02 Hz)	~0.002 (0.02 Hz)	~1
[2]	Chitosan/ MWCNT	—	—	$EMIBF_4$/ glycerol/ chitosan	—	±3 square	30×5× 0.17	~0.05 (0.5 Hz)	—	—
[3]	SWCNT/ $BMIBF_4$/ PVDFHFP	—	—	$BMIBF_4$/ PVDFHFP	—	±3.5 square	15×1× 0.28	0.257 (0.01 Hz)	—	—
[4]	(Long SWCNT)/ EMITFSI/ PVDFHFP	17	0.156	EMITFSI/ PVDFHFP	<0.156	±2.5 square	15×1× ~0.06	~0.091 (10 Hz)	—	—
[5]	CNT/ PVDF	—	—	$EMIBF_4$/ PVDF	—	±2.5	25×2.5× 0.08	~0.032 (0.1 Hz)	0.552 (0.1 Hz)	—
[5]	Graphene /PVDF	—	—	$EMIBF_4$/ PVDF	—	±2.5	25×2.5× 0.08	~0.096 (0.1 Hz)	0.768 (0.1 Hz)	—
[5]	Graphdiyne /PVDF	—	—	$EMIBF_4$/ PVDF	0.420	±2.5	25×2.5× 0.08	~0.624 (0.1 Hz)	1.35 (0.1 Hz)	—
[6]	Carbon nitride/PVDF /EMImBF4	—	—	$EMIBF_4$/ PEO/NBR	—	±3 (square)	20×2.5× ~0.085	~0.62 (0.001 Hz)	0.23 (0.01 Hz, 4 V)	—
[7]	(BP-CNT) /CNT	23	0.95	$EMIBF_4$/ PVDF-HFP	0.246	±2.5 (square)	23×5× 0.115	0.668 (0.1 Hz)	2.4	—
[8]	MXene	—	—	H_2SO_4/ PVA	0.04	±0.6 triangular	5×40× ~0.075	0.433/0.025 (0.001/0.1 Hz)	—	—
[9]	MXene/3D (PS-MXene)	~15	3.3	$EMIBF_4$/ PVDF	0.246	±1.5 (square)	20×5× 0.095	0.787 (0.1 Hz)	—	—
[10]	Methyl-cellulose /MXene	53.2	12.4	5.6 M LiBr/ TPU/CMP	1.93	±1 triangular	22×3× 0.123	0.541/0.320/0 .0364 (0.001/0.01/0. 1 Hz)	0.826 (DC 1 V)	4.7
This work	**TBA-MXene**	54.6	9.49	5.6 M LiBr/ TPU/CMP	1.69	±1 triangular	22×3× 0.10 (L_f [c] = 20)	**0.771**/0.431/0 .0566 (0.001/0.01/0. 1 Hz)	**1.01** (DC 1 V in 10 s)	**7.55**
							8×3× 0.10 (L_f = 6)	—	**1.81**	**51.5**

Note: [a] length×width×thickness; [b] Not available; [c] free length (mm)

Supplemental Movie 1. The profile change of a TBA-MXene cluster observed by liquid cell TEM during scanning from 0 to -0.8 V vs Pt at 20 mV s^{-1}.

Supplemental Movie 2. The deformation of a TBA-MXene-based IECA working in air under a triangular voltage of ±1 V and 0.01 Hz (40 mV s^{-1}) (Speed: ×15).

Supplemental Movie 3. The soft tweezer based on two IECAs opens at 1 V and grasp the flower at -1 V and hold it firmly even the voltage is reduced to 0 V. The real-time voltage is shown at the top right corner. (Speed: ×6)

References

[1] Y. Yan, T. Santaniello, L. G. Bettini, C. Minnai, A. Bellacicca, R. Porotti, I. Denti, G. Faraone, M. Merlini, C. Lenardi, *Adv. Mater.* **2017**, 29, 1606109.

[2] L. Lu, W. Chen, *Adv. Mater.* **2010**, 22, 3745.

[3] T. Fukushima, K. Asaka, A. Kosaka, T. Aida, *Angew. Chem. Int. Ed.* **2005**, 44, 2410.

[4] K. Mukai, K. Asaka, T. Sugino, K. Kiyohara, I. Takeuchi, N. Terasawa, D. N. Futaba, K. Hata, T. Fukushima, T. Aida, *Adv. Mater.* **2009**, 21, 1582.

[5] C. Lu, Y. Yang, J. Wang, R. Fu, X. Zhao, L. Zhao, Y. Ming, Y. Hu, H. Lin, X. Tao, Y. Li, W. Chen, *Nat. Commun.* **2018**, 9, 752.

[6] G. Wu, Y. Hu, Y. Liu, J. Zhao, X. Chen, V. Whoehling, C. Plesse, G. T. M. Nguyen, F. Vidal, W. Chen, *Nat. Commun.* **2015**, 6.

[7] G. Wu, X. Wu, Y. Xu, H. Cheng, J. Meng, Q. Yu, X. Shi, K. Zhang, W. Chen, S. Chen, *Adv. Mater.* **2019**, 31, 1806492.

[8] D. Pang, M. Alhabeb, X. Mu, Y. Dall'Agnese, Y. Gogotsi, Y. Gao, *Nano Lett.* **2019**, 19, 7443.

[9] T. Wang, T. Wang, C. Weng, L. Liu, J. Zhao, Z. Zhang, *Nano Res.* **2021**, 14, 2277.

[10] S. Chen, J. H. Ciou, F. Yu, J. Chen, J. Lv, P. S. Lee, *Adv. Mater.* **2022**, 34, 2200660.